

Predicting interface and spin states in armchair graphene nanoribbon junctions

Sofia Sanz^{1,*} and Daniel Sánchez-Portal^{1,†}

¹ *Centro de Física de Materiales (CFM) CSIC-UPV/EHU, E-20018, Donostia-San Sebastián, Spain*
(Dated: July 21, 2025)

We present a theoretical analysis of interface states emerging at junctions between armchair graphene nanoribbons of varying widths. By exploring diverse width combinations and junction geometries, we demonstrate that predicting the precise number of interface states requires considerations beyond the topological classification alone; specifically, the width differences and bonding configuration at the interface play crucial roles. For junctions involving ribbons with small gaps, we further examine how an applied strain affects their topological properties and, consequently, the interface states formed. The spin states at these junctions are investigated using the mean-field Hubbard model, revealing how the magnetic behavior at the interface depends on the number of localized states present. These results are summarized in a series of “rules of thumb” to predict the number of localized states and the magnetic moment at the junction. Our findings contribute to understanding and engineering localized states in graphene-based devices, providing guidelines for manipulating electronic and magnetic properties through structural design.

I. INTRODUCTION

Graphene nanoribbons (GNRs) have emerged as key building blocks for advanced nanoelectronic, spintronic, and optoelectronic devices, owing to their unique physical properties, such as highly tunable band structures and edge-dependent electronic states [1–15]. In addition to their electronic properties, the advances in experimental techniques enable the fabrication of atomically precise GNRs with tailored widths [16, 17]. Besides their intrinsic properties, these laterally confined, semiconducting strips of graphene exhibit a fascinating topological nature, which has become a major area of focus in recent years [18–25]. In the seminal paper by Cao et al., the authors showed for the first time that the topological phase of armchair GNRs (AGNRs) with spatial symmetry is dictated by their width, edge shape and terminating unit cell [18]. In this regard, GNRs can be characterized by a Z_2 invariant which takes a value of either 0 or 1 and classifies them as topologically trivial or non-trivial, respectively [18, 26]. Topologically non-trivial semiconducting AGNRs can host highly robust symmetry-protected in-gap states localized at the ribbon terminations, while maintaining an insulating bulk [18]. The Z_2 invariant can be obtained from the Zak phase, derived from the integration of the Berry connection of the occupied bands across the 1D Brillouin zone (BZ) [18, 27]. Later, the Z_2 invariant was generalized into the chiral-phase index (Z), which relies on the chiral symmetry rather than time-reversal symmetry, providing a broader classification scheme for GNR topological phases [21]. It is now well-established that the width, length, and termination geometry of AGNRs strongly influence their topological invariants (Z_2 and Z) and the emergence of localized in-gap end states (ESs) [22, 23, 25, 28–30]. For instance,

wider AGNRs host multiple topological transitions, resulting in the appearance of multiple ESs [22, 25, 30], where the topological invariant $|Z|$ corresponds to the number of these states [21, 22].

The interest on the topology of single GNRs, has naturally evolved to the novel quantum phases that emerge by coupling sections of GNRs of different topological character. For instance, AGNR heterojunctions provide a platform to explore rich physical phenomena arising from the interplay of topology and geometry, since interfaces between topologically distinct AGNRs characterized by differing Z_2 or Z values host half-filled, localized bound states within the energy gap [19, 20, 31–40]. In this sense, similarly to single GNRs, AGNR superlattices can be classified into topological or trivial junctions, where the key ingredient is the difference between the widths of the AGNRs [21, 22]. However, the precise number of interface states and the role of carbon-carbon (C-C) bonding at the junction remain less well understood. While it has been suggested that bonding at the interface plays a crucial role [41], prior studies typically focus on fixed bonding configurations and lack a systematic exploration of how variations in bonding affect the formation of localized states. Moreover, the magnetic properties associated with these localized states at the interface, essential for spintronic applications, have not been comprehensively addressed.

We bridge these gaps by performing a systematic theoretical study of AGNR heterojunctions of varying widths, alignments, and some geometrical deformations. Strain, for example, is known to strongly influence key electronic properties such as magnetism and topology in GNRs [29, 42]. Using a combination of tight-binding (TB) and mean-field Hubbard (MFH) calculations, we explore the role of interface bonding, topology and width difference, with special focus on the number of localized states, while also investigating the effects of strain and Coulomb interactions. The computed spin configurations at the junction are benchmarked against density functional theory (DFT) calculations, which confirm the validity of our ap-

* sofia.sanzwuhl@ehu.eus

† daniel.sanchez@ehu.eus

proach. From these results, we derive predictive “rules of thumb” that relate interface structure to the number of interface states, providing useful design guidelines for AGNR-based circuits with tunable electronic and magnetic properties.

This paper is organized as follows: In Sec. II, we describe the Hamiltonian used to model the systems under investigation. In Sec. III we rationalize the emergence of ESs in AGNRs as a function of the ribbon width. In Sec. IV, we present our findings, starting with the analysis of interface states in AGNR heterojunctions for different bonding configurations (Sec. IV A). In Sec. IV B we systematically analyze the number of states at different junction interfaces for a wide variety of width combinations. In Sec. IV C we derive an effective model to predict the number of interface states related to the interface geometry. We then explore how interface states behave under geometrical deformations by applying a uniaxial-strain (Sec. IV D), followed by an examination of the magnetic ground state (Sec. IV E) and the first excited magnetic states (Sec. IV F) at the interface of these heterojunctions. Finally, Sec. V summarizes the key findings of the manuscript.

II. COMPUTATIONAL FRAMEWORK

The Hamiltonian of the AGNR heterojunction (see Fig. 1) is defined by $H = H_\ell + H_r + V$. Where $H_{\ell,r}$ is the Hamiltonian of the left and right AGNR, respectively, and V is the coupling matrix between them at the interface. The electronic properties of these junctions are modeled using the well-established one orbital MFH Hamiltonian [43], which has proven effective in describing these sp^2 hybridized systems according to experimental results and other more accurate descriptions, such as DFT calculations [44–47]. The Hamiltonian is expressed in terms of microscopic parameters as:

$$H = \sum_{\langle ij \rangle \sigma} t c_{i\sigma}^\dagger c_{j\sigma} + U \sum_{i\sigma} \langle n_{i\sigma} \rangle n_{i\bar{\sigma}}, \quad (1)$$

where U represents the on-site Coulomb repulsion parameter, accounting for the electron-electron interaction within the same p_z orbital. The operators $c_{i\sigma}$ and $c_{i\sigma}^\dagger$ denote the annihilation and creation operators, respectively, of an electron at site i with spin index $\sigma = \{\uparrow, \downarrow\}$, while $n_{i\sigma} = c_{i\sigma}^\dagger c_{i\sigma}$ is the corresponding number operator. We adopt the first-nearest neighbor (1NN) TB model where the hopping parameter is $t = 2.7$ eV [48] for atoms i, j separated by a first-neighbor distance of $d_{\langle ij \rangle} = 1.42$ Å. This simple yet efficient description allowed us to systematically explore a wide variety of junctions of different widths and interface configurations.

The TB results (with $U = 0$) presented below, are obtained for very large finite systems. In contrast, self-consistent calculations with $U > 0$ were performed imposing open boundary conditions and employing the

Green’s function methodology to solve the Schrödinger equation. In this way, we can effectively isolate the different spin states at the junctions from interactions with magnetic moments that can appear at the other terminations of finite systems. For this purpose, we use our custom Python library HUBBARD [49] which relies on SISL [50]. The details for this implementation, can be found in [49, 51].

III. END STATES OF AGNRs

The emergence and features of ESs in finite-length AGNRs can be intuitively understood by decomposing their band structure into transverse modes [5], each of which can be effectively described by a Su-Schrieffer-Heeger (SSH) chain [52]. This representation, discussed in Ref. [30] and in Sec. S1 of the Supplemental Material (SM) [53], enables a mode-by-mode analysis of the topological character and the associated emergence of ESs in AGNRs. Such mapping is exact within a π -orbital TB model with 1NN interactions. The transverse modes correspond to a set of quantized wave vectors k_n , determined by the boundary conditions of an AGNR of width W (W -AGNR), defined in Fig. 1a:

$$k_n = \frac{2\pi n}{(W+1)a}, \quad n = 1, \dots, \lfloor \frac{W+1}{2} \rfloor. \quad (2)$$

For odd W , this collection of allowed transverse modes includes $k_{(W+1)/2} = \frac{\pi}{a}$, which gives rise to two non-dispersive bands in their band structure, and whose wavefunctions are strongly localized in the wider parts of the AGNR unit cell [30]. The rest of the transverse modes correspond to dispersive bands that can be effectively described by SSH-like chains with intra- and inter-cell hopping amplitudes given by $t_{\text{intra}}(k_n) = 2t \cos(k_n \frac{a}{2})$ and $t_{\text{inter}}(k_n) = t$, respectively (see Sec. S1 [53]). From this representation, each AGNR band exhibits a nontrivial topological character its the corresponding k_n satisfies

$$2t \cos(k_n \frac{a}{2}) < t. \quad (3)$$

This condition implies that the non-trivial bands correspond to those $k_n > \frac{2\pi}{3a}$. For finite AGNRs with even W there is only one possible zigzag termination. Each topological transverse mode contributes with one topological state per end and, therefore, the number of ESs (M) is equal to the number of topological k_n . For odd values of W , the precise value of M depends on the terminating unit cell of the ribbon. As mentioned before, the topological invariant $|Z|$ is equal to M [21, 22].

It should be noted that the emergence of ESs in AGNRs depends on a minimum length requirement to ensure sufficient decoupling of ESs appearing at different ends of the ribbon [25]. This required length is determined by the decay length associated with the respective k_n , and related to the corresponding band gap $E_g(k_n) = 2t|1 - 2 \cos(k_n \frac{a}{2})|$.

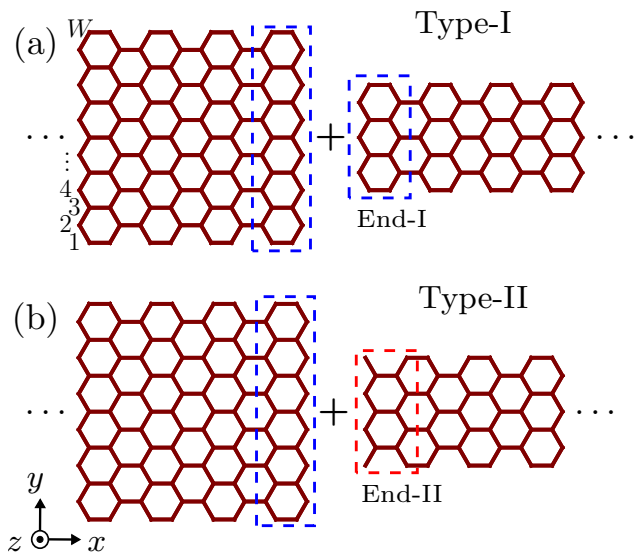


FIG. 1. Atomic structure of the two possible junctions for an example case consisting of a 13-AGNR (left) and a 7-AGNR (right). (a) Type-I junction, formed by two End-I unit cells (blue dashed rectangles). The AGNR width (W) is defined as the number of atoms across, as indicated in panel (a). (b) Type-II junction, formed by one End-I (blue dashed rectangle) and one End-II (red dashed rectangle) termination cells. Inset axes in the lower part of panel (b) define the xyz directions.

Here we investigate the two types of terminations depicted in Fig. 1, End-I [depicted in blue in panels (a,b)] and End-II [depicted in red in panel (b)]. The ES derived from $k_{(W+1)/2} = \frac{\pi}{a}$ only appears for the End-II termination, resulting in $M_{II} = M_I + 1$ (see Sec. S1 [53]). Because of this somewhat richer scenario, that gives rise to two different types of heterojunctions, we will focus below on odd values of W . However, results for End-I terminations can be directly generalized to cases with even W .

Two types of junctions are considered: Type-I (Fig. 1a), conformed by two End-I unit cells, and Type-II (Fig. 1b), conformed by one End-I and one End-II unit cells. As the two types of AGNR terminations exhibit different bulk-boundary correspondences, their combination is expected to influence both the emergence and nature of the interface states [18, 22]. Note that Type-II junctions only make sense for fully-coupled configurations.

IV. RESULTS

A. Interface states and bonding configuration

In this section we investigate the formation of interface bound states that emerge at the junctions of AGNRs of varying interface connections, characterized by their rel-

ative vertical alignments (*i.e.*, different number of C-C bonds at the interface). We start by characterizing a Type-I junction formed by a 21- and a 19-AGNR (21-19) at the interface position, x_{int} (see Fig. 2a). Both ribbons share the same topological classification ($Z = 3$) and possess three ESs, $M_\ell = M_r = 3$, where ℓ (r) stands for the left (right) AGNR in Fig. 1. We examine five different vertical alignments, where the number of C-C bonds at the interface ranges from one to nine in steps of two [see geometries (i-v) in Fig. 2b]. For each geometry, we investigate the behavior of the interface states by analyzing the local density of states (LDOS) at x_{int} , in Fig. 2c. We evaluate the LDOS as a function of the coupling between the two ribbons, t_{int} (see Fig. 2a), within an energy window of ± 0.65 eV. In this sense, for $t_{\text{int}} = 0$, we recover the results for two finite unconnected ribbons (six states at the junction resulting from the contribution of M_ℓ and M_r), while as t_{int} increases, some of these states hybridize and move away from zero energy. More details for these calculations are provided in Sec. S2 [53].

For configurations with fewer bonds (one to three), we observe high LDOS at $E = 0$ irrespective of t_{int} in Fig. 2c(i-iii), indicating the presence of unhybridized zero-energy modes at the interface. In contrast, configurations with higher connectivity (more than seven bonds) display no zero-energy states, as all localized states are hybridized at the interface, as seen in Fig. 2c(iv-v).

Following the dispersion of the different peaks as a function of t_{int} is also quite informative. For instance, in panel Fig. 2c(i) two states move away from $E = 0$ as t_{int} increases, indicating partial hybridization, while a persistent peak at $E = 0$ reflects remaining unhybridized states. The two dispersing peaks eventually leave the in-gap region (delimited by the red-dashed lines), losing intensity progressively. Note that, in absence of Coulomb interactions (*i.e.*, $U = 0$), electron-hole symmetry is perfectly preserved. In panel Fig. 2c(ii) we observe four states lying at $|E| > 0$, meaning two from each AGNR hybridize, while the remaining ones stay at zero energy. Two of them hybridize very strongly, leaving the in-gap region for $t_{\text{int}} \sim t/2$, while the other two exhibit a slower linear dispersion, developing an appreciable splitting for $t_{\text{int}} \sim 3t/2$. In panel Fig. 2c(iii) there are four states that hybridize more rapidly than in panel Fig. 2c(ii), as we observe that the second set of lines abandon the in-gap energy window for $t_{\text{int}} \sim t/2$. The two remaining states show some degree of hybridization but their energy splitting remains negligible over the whole studied range of t_{int} . As the number of C-C bonds increases further, zero-energy LDOS features vanish due to the energy splitting of the interface states. This is evident in panels Fig. 2c(iv-v), where all six interface states are hybridized, and no zero-energy features remain. In the case of geometry (v), the two AGNRs are fully coupled with nine interfacial bonds. In this case we observe that all states have merged the continuum bands for relatively low values of t_{int} . As expected, our results reveal that the number of states that hybridize and the pace at which

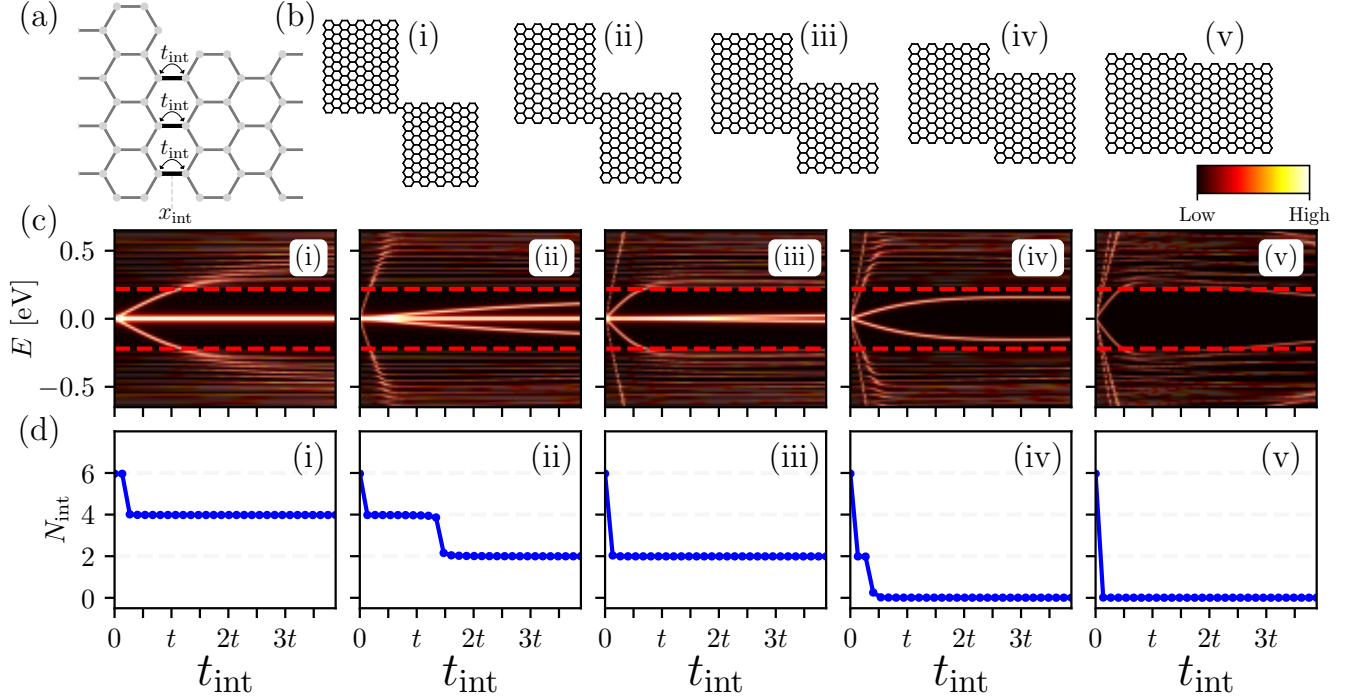


FIG. 2. Interface states analysis for a finite 21-19 Type-I heterojunction with different vertical alignments. (a) Sketch of the carbon backbone structure at the junction, highlighting the interfacial hopping elements (t_{int}) and the horizontal position of the interface (x_{int}). (b) Geometries (i-v) with one to nine C-C bonds at the interface in steps of two, respectively. (c) LDOS map at x_{int} within an energy window of ± 0.65 eV for each (i-v) geometry shown in panel (b) as a function of t_{int} , with $t = 2.7$ eV elsewhere. Red dashed lines indicate the band-gap of the system ($\pm E_g/2$). Inset colorbar indicates the low and high LDOS regions in (c). (d) Number of interface states (N_{int}), as a function of t_{int} , for each geometry (i-v) shown in panel (b), calculated as explained in Sec. S2 [53]. These calculations were performed with $U = 0$.

they move away from zero energy depend on the precise connectivity between the AGNRs.

To quantify the number of states at the interface, N_{int} , we sum the projected density of states (PDOS) around the junction area, accounting for the decay length of the ESSs, and integrate within a narrow energy window of ± 50 meV around $E = 0$. The choice of this energy cutoff ensures that each state remains spectrally isolated from the bulk continuum while capturing its full spectral weight. For example, in the 21-19 heterojunction, the smallest band gap among the two ribbons is that of the 21-AGNR, with $E_g \sim 440$ meV, making the chosen window well within the gap. Further computational details are provided in Sec. S2 [53].

In Fig. 2d(i-v) we plot N_{int} for each geometry (i-v) and coupling strength t_{int} . Inspecting Fig. 2d(i) we observe that, for the case with one single C-C bond, there are four states at the interface for $t_{\text{int}} > 0$. This result is in agreement with the LDOS analysis [Fig. 2c(i)] where only two states out of six are coupled, which yields four unhybridized states at the interface. Similarly, for the case with three C-C bonds at the interface [Fig. 2d(ii)], we find that $N_{\text{int}} = 4$ for $t_{\text{int}} < 3t/2$, while it decreases to $N_{\text{int}} = 2$ for $t_{\text{int}} > 3t/2$. In this case, the larger contact area facilitates this hybridization, but its extent depends

sensitively on the value of t_{int} . For the geometry with five C-C bonds, $N_{\text{int}} = 2$ for $t_{\text{int}} > 0$, as seen in panel Fig. 2d(iii). These results are again consistent with the evolution of hybridized states observed in Fig. 2c(ii-iii) at different coupling strengths. In panels Fig. 2d(iv-v) we observe that N_{int} rapidly goes to zero, in full agreement with the observed absence of LDOS at $E = 0$ in panels Fig. 2c(iv-v). A similar analysis for 25-15 junctions is presented in Fig. S5 [53], illustrating the dependence of N_{int} on the interfacial bonding in a different case.

B. Fully coupled Type-I vs. Type-II interfaces

In this section, we analyze how the number of interface states N_{int} depends on the junction termination (Type-I vs. Type-II) and the ribbon widths, focusing on fully coupled configurations (*i.e.*, with the maximum number of C-C bonds). We systematically computed N_{int} for a wide range of width combinations, and summarize the results in Tables I and II.

Table I summarizes N_{int}^I obtained for various fully coupled Type-I junctions formed by AGNRs of different widths. These trends are corroborated in Fig. S6 [53], where we plot N_{int} as a function of t_{int} for the junctions

Widths	3	7	9	13	15	19	21	25
7	1							
9	1	0						
13	2	1	1					
15	2	1	1	0				
19	3	2	2	1	1			
21	3	2	2	1	1	0		
25	4	3	3	2	2	1	1	
27	4	3	3	2	2	1	1	0

TABLE I. **Type-I heterojunction**: number of interface states of fully-coupled Type-I heterojunctions (N_{int}^I) formed by AGNRs of different widths, calculated with $U = 0$. The rows correspond to the left (wider) AGNR while the columns correspond to the right (narrower) AGNR, as sketched in Fig. 1a.

Widths	3	7	9	13	15	19	21	25
7	0							
9	0	1						
13	1	0	0					
15	1	0	0	1				
19	2	1	1	0	0			
21	2	1	1	0	0	1		
25	3	2	2	1	1	0	0	
27	3	2	2	1	1	0	0	1

TABLE II. **Type-II heterojunction**: number of interface states of fully-coupled Type-II heterojunctions (N_{int}^{II}) formed by AGNRs of different widths, calculated with $U = 0$. The rows correspond to the left (wider) AGNR while the columns correspond to the right (narrower) AGNR, as sketched in Fig. 1b.

presented in Table I. Similarly, Table II summarizes the resulting number of interface states for Type-II heterojunctions. Interestingly, we have verified that the results in Table I and Table II are independent on the specific geometry of the contact and hold as far as the ribbons are fully connected.

By comparing the two Tables I and II, we observe that in most of the cases, Type-II junctions host one fewer interface state than their Type-I counterparts. There are a few exceptions (highlighted in blue in Table II) where $N_{\text{int}}^I = 0$ and yet $N_{\text{int}}^{II} = 1$, as seen in junctions like 9–7, 13–15, 19–21, and 25–27. These results can be encapsulated in the expression $N_{\text{int}}^{II} = |N_{\text{int}}^I - 1|$.

C. Effective model for interface states counting

To explain the results of Tables I and II, we developed an effective model that yields an expression for N_{int} in terms of the AGNR widths, termination types, and bonding configuration.

As a starting point, the coupling between the two AGNRs (V) is treated perturbatively, since it involves only a few hopping terms between the terminal sites of the ribbons. In fact, the coupling strength between bulk states

scales with the length of the AGNRs along the x -axis (L) as $\propto L^{-1}$, due to wavefunction normalization, assuming L is equal for both ribbons. Therefore, in this approach, we can disregard the hybridization between extended states and consider only the coupling between ESs localized at the interface. For these calculations, we use $L = 40$ unit cell repetitions along the x -axis for each AGNR (*i.e.*, a total length of ~ 338 Å), to ensure the weak coupling regime. In this treatment, the low energy spectrum of the junction is computed from the effective Hamiltonian obtained by projecting the TB Hamiltonian of the junction in the subspace of ESs of the left and right AGNRs ($\{\Phi_\ell^{\text{ES}}\}$ and $\{\Phi_r^{\text{ES}}\}$, respectively). Since $\langle \Phi_\ell^{\text{ES}} | H_{\ell,r} | \Phi_r^{\text{ES}} \rangle = 0$, the resulting effective Hamiltonian reads

$$H_{\text{eff}} = \begin{pmatrix} 0 & \mathcal{V} \\ \mathcal{V}^\dagger & 0 \end{pmatrix}, \quad \mathcal{V} \equiv \langle \Phi_\ell^{\text{ES}} | V | \Phi_r^{\text{ES}} \rangle. \quad (4)$$

This effective model and the full TB spectrum are compared in Sec. S4 and Fig. S7 [53], showing excellent agreement in the low energy range.

The matrix \mathcal{V} captures the effective coupling between ESs. Physically, each non-zero singular value of \mathcal{V} represents a bonding/antibonding pair obtained from linear combinations of ESs from each ribbon. The rank of this matrix, thus, gives the number of hybridizing pairs of such states. In principle, each hybridized pair removes two zero-energy modes from the spectrum. In practice, a numerical threshold to identify the non-zero singular values is imposed in order to determine $\text{rank}(\mathcal{V})$, analogously to the energy window needed to compute N_{int} in Sec. IV A. Since each AGNR contributes respectively with $M_{\ell,r}$ ESs to the interface, we arrive at the following expression for the number of interface states:

$$N_{\text{int}}^T = M_\ell^T + M_r^T - 2 \cdot \text{rank}(\mathcal{V}_T). \quad (5)$$

The index $T = \{I, II\}$ here differentiates the junction and unit-cell type. It is omitted when unambiguous or for general features for both types. As mentioned before, in this article we only consider End-I for the left AGNR.

Moreover, $\text{rank}(\mathcal{V})$ reaches its maximum value for the case where the number of C-C bonds at the interface is maximum. In particular, we have observed that for fully-coupled junctions $\text{rank}(\mathcal{V}) = \min(M_\ell, M_r)$. Therefore, the number of interface states boils down to:

$$N_{\text{int}}^{T,\text{full}} = |M_\ell^T - M_r^T|, \quad (6)$$

as previously inferred [21].

Eqs. 5 and 6 are general expressions valid for both Type-I and Type-II heterojunctions, and can be used to easily understand the results found in Sec. IV B. Let us first consider the case where $N_{\text{int}}^I \neq 0$. For Type-II junctions (which are fully coupled by definition), the right AGNR is terminated with End-II, and hence, contains one additional ES compared to its End-I counterpart, *i.e.*, $M_r^{II} = M_r^I + 1$ (see Sec. III). This also increases the rank of the coupling matrix by one, $\text{rank}(\mathcal{V}_{II}) =$

$\text{rank}(\mathcal{V}_I) + 1$. Substituting these two expressions into Eq. (5), we recover the relation $N_{\text{int}}^{II} = |N_{\text{int}}^I - 1|$. In the special case where $N_{\text{int}}^I = 0$, the rank remains the same for both junction types, since it is limited by the smaller number of ESs, here M_ℓ^I , since $M_r^{II} = M_\ell^I + 1$. Substituting again into Eq. (5), we find $N_{\text{int}}^{II} = 1$, in agreement with the data in Sec. IV B. This behavior is verified by explicitly computing $\text{rank}(\mathcal{V}_T)$ as a function of t_{int} , as we show for two example junctions, in Fig. S8 [53].

D. Interface states under applied strain

The electronic structure of AGNRs of width $W = 3p+2$ (with p an integer)—which appear metallic within the 1NN description [4, 46]—is highly sensitive to structural deformations or environmental effects such as, *e.g.*, interaction with a surface underneath. More accurate theoretical models have demonstrated that these ribbons are, in fact, semiconducting [4, 46], in agreement with experimental observations [29, 54, 55]. Beyond their band gap behavior, other electronic features also depend on the atomic-scale details. For instance, the topological character of a 5-AGNR depends on the relation between the hopping parameters resulting from the relaxed geometry [29]. Here, we investigate how applying uniaxial strain (sketched in Fig. 3a) can alter the properties and topological nature of the AGNRs, and therefore, the precise number of interface states at the junctions.

To understand how this geometrical deformation affects the interface states, we employ a minimal model in which strain is introduced via a dimensionless parameter δ that modifies the hopping amplitude along the direction parallel to the ribbon's axis (t'), such that $t' = t(1 + \delta)$. We assume that only the hopping terms strictly along the x -direction are affected by strain. In this sense, $\delta > 0$ corresponds to compression while $\delta < 0$ corresponds to elongation. We note that under compressive conditions, the ribbon may deviate from planarity, and capturing such distortions would require a more sophisticated structural model. This simplified model is not meant to describe detailed structural relaxation but rather to explore qualitative behaviors.

The modified hopping leads to an adjusted condition for the emergence of topological modes, analogous to Eq. (3). This expression reads (see Sec. S1 [53]):

$$2t \cos(k_n \frac{a}{2}) < t'. \quad (7)$$

In Fig. 3 we explore the topological phase diagram of periodic 5-, 11- and 15-AGNRs, as well as the interface states in 15–5 and 15–11 finite heterojunctions, as a function of the applied strain. Panels (b) and (c) show the evolution of E_g as a function of the strain parameter δ for the 5- and 11-AGNR, respectively. The color identifies the topological invariant $Z(\delta)$, calculated as the number of ESs [21, 22]. The vertical gray dashed lines mark the critical points where topological transitions occur. We

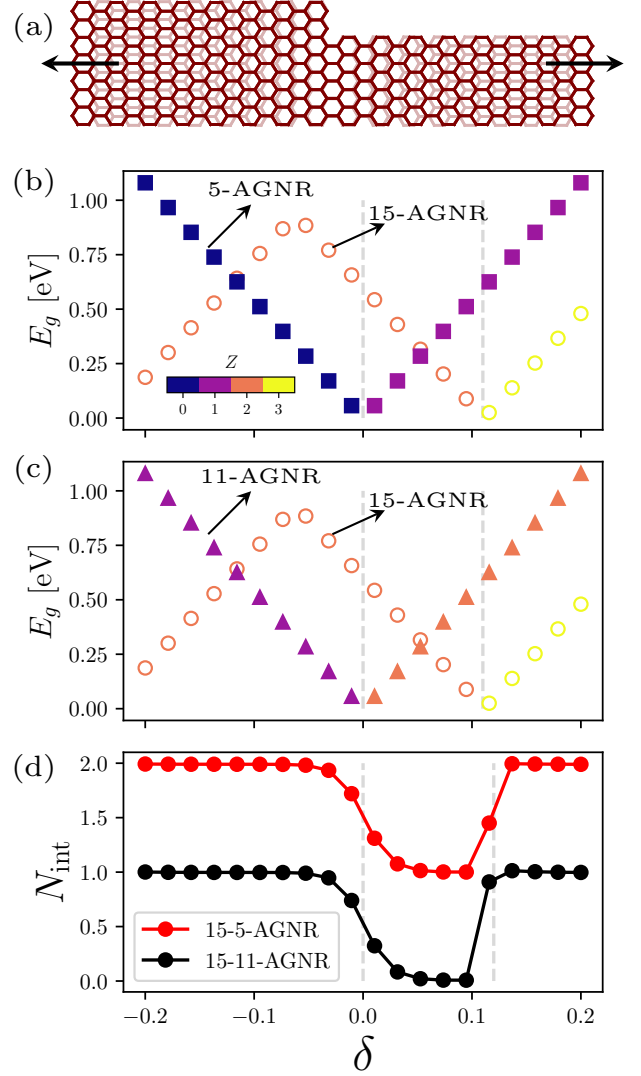


FIG. 3. Topological phase space as a function of the applied strain. (a) Sketch of a strained 15-11 Type-I junction. (b) Band gap energy, E_g , as a function of δ for a 5-AGNR (filled squares) and a 15-AGNR (open circles). (c) E_g for an 11-AGNR (filled triangles) and a 15-AGNR (open circles). The color (blue, purple, orange, yellow) identifies the topological character Z , as indicated by the inset colorbar in panel (b). (d) N_{int} for each δ for the 15-5 and 15-11 heterojunction, displayed in red and black lines, respectively. These calculations were performed with $U = 0$. The light gray dashed lines indicate the δ values at which there are topological phase transitions.

observe that both the 5-AGNR [filled squares in panel (b)] and the 11-AGNR [filled triangles in panel (c)] undergo a topological transition at $\delta = 0$, which coincides with the band gap closure. Specifically, the 5-AGNR changes from $Z(\delta < 0) = 0$ to $Z(\delta > 0) = 1$, while the 11-AGNR evolves from $Z(\delta < 0) = 1$ to $Z(\delta > 0) = 2$, given that the 11-AGNR has one more topological k_n than the 5-AGNR. This behavior can be understood from the cri-

terion in Eq. (7): as δ decreases, fewer transverse wave vectors k_n satisfy the inequality, reducing the number of topological modes. Conversely, increasing δ expands the range of k_n values that meet the condition. For comparison, we also include the band gap and topological index of a 15-AGNR (open circles) in Fig. 3(b,c), which undergoes a transition at $\delta = 0.12$, and its classification changes from $Z = 2$ to $Z = 3$.

Panel Fig. 3d displays the evolution of N_{int} for a 15-5 (red curve) and a 15-11 Type-I junction (black curve) as a function of δ . The vertical dashed lines indicate the topological transitions of the individual ribbons, as discussed above. Starting with the 15-5 heterojunction, we can see that in the region $\delta < 0$ there are two states at the interface, since the 15-AGNR contributes with $M_\ell = 2$ while the 5-AGNR contributes with $M_r = 0$, giving $N_{\text{int}} = |2 - 0| = 2$. In the intermediate region $0 < \delta < 0.12$, the 5-AGNR transitions to $M_r = 1$, while the 15-AGNR remains at $M_\ell = 2$, resulting in $N_{\text{int}} = |2 - 1| = 1$. For $\delta > 0.12$, both ribbons have changed their topological phase, yielding $M_\ell = 3$ and $M_r = 1$, so that $N_{\text{int}} = |3 - 1| = 2$. Similarly, in the case of the 15-11 heterojunction, in the region $\delta < 0$, the 11-AGNR contributes with $M_r = 1$, while the 15-AGNR contributes with $M_\ell = 2$, giving a result of $N_{\text{int}} = |2 - 1| = 1$. In the range $0 < \delta < 0.12$ both ribbons share the same topological index $Z = 2$, and therefore $M_\ell = M_r = 2$, yielding $N_{\text{int}} = |2 - 2| = 0$ states at the interface. For $\delta > 0.12$ there are $N_{\text{int}} = |3 - 2| = 1$ states at the interface, since the 15-AGNR contributes with $M_\ell = 3$. This analysis highlights how geometric deformations, such as the applied strain, provide a tunable handle to control the number of interface states in AGNR heterojunctions.

E. Magnetic ground state at the interface

After establishing the dependence of interface states on ribbon widths, alignments, and bonding geometries, we now turn to a key consequence of their presence: the emergence of localized magnetic moments when Coulomb interactions are included (*i.e.*, $U > 0$) in the MFH model [Eq. (1)]. We study both Type-I and Type-II junctions, exploring various vertical alignments to uncover the interplay between geometry and magnetism at the interface. To compute the magnetic state at the interface, we employ open boundary conditions. Thus, spin-polarized states are calculated self-consistently using the Green's function formalism, as described in Sec. II. We use a sufficiently long scattering region ($L = 15$ unit cells for each AGNR) to ensure that the electrodes, placed at the free ends of each AGNR, exhibit bulk-like behavior. This eliminates the magnetic moments at those terminations, isolating the magnetic response at the junction interface.

We start by computing the magnetic ground state (GS) of a junction with $N_{\text{int}}^I \neq 0$ to unveil the magnetic properties of the localized interface states. For that, we choose

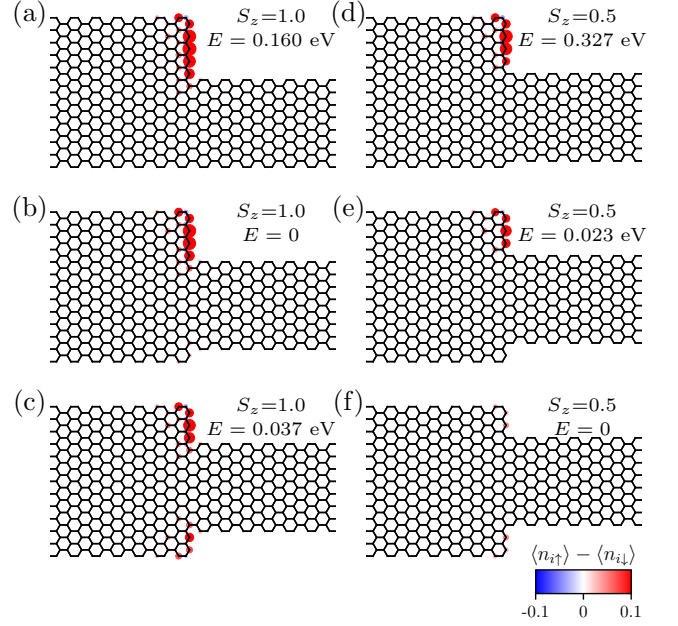


FIG. 4. Spin density distribution in fully coupled 25-15 Type-I and Type-II junctions. The total energy E and spin moment S_z are annotated in each panel. (a-c) Type-I junctions with three different vertical alignments, respectively. The energy reference corresponds to the most favorable geometry shown in panel (b). (d-f) Type-II junctions with three different vertical alignments, respectively. Here we take the energy reference of panel (f) as it is the most favorable case. Size and color of the blobs at each site indicates both the magnitude and sign of the spin density, as indicated by the inset colorbar, common for all panels. These calculations were performed with open boundary conditions and $U = 3$ eV.

fully-coupled junction formed of a 25- and a 15-AGNR (25-15), and consider different vertical alignments. For this junction, $N_{\text{int}}^I = 2$ and $N_{\text{int}}^{II} = 1$ (see Tables I-II). Fig. 4 shows the resulting spin density distribution for 25-15 junctions, across different vertical alignments for both Type-I [panels (a-c)] and Type-II [panels (d-f)] configurations. Both the total spin moment S_z and the total energy E for each junction are annotated in each panel. Numerically, the total spin moment is computed as $S_z = \sum_i s_z(i)$, where the atomic spin polarization is given by

$$s_z(i) = \frac{1}{2} (\langle n_{i\uparrow} \rangle - \langle n_{i\downarrow} \rangle). \quad (8)$$

The sum runs over all atoms in the scattering region, as we employed open boundary conditions. Note that the sign of $s_z(i)$ depends on the arbitrary choice for spin orientation; thus, only relative spin alignments have physical significance.

Remarkably, for all alignments—including partially coupled cases (see Fig. S9 [53])—the magnitude of the GS spin moment remains robust and follows a clear rule:

$$|S_z^{\text{GS}}| = \frac{1}{2} N_{\text{int}}^{\text{full}}, \quad (9)$$

where $N_{\text{int}}^{\text{full}}$ stands for the number of interface states for *fully-coupled* junctions. For the 25-15 Type-I junctions, this yields $S_z = 1$, while for 25-15 Type-II junctions, $S_z = 0.5$. We compare our results against DFT calculations (see Appendix A), which confirm the validity of our approach.

In second place, we observe that the total energy of the system varies depending on the vertical alignment of the ribbons, as displayed in Fig. 4 for both Type-I and Type-II junctions. The total energy for each configuration is given relative to the lowest-energy solution within each class of junctions. For instance, for 25-15 Type-I junctions, geometry of panel (b) corresponds to the most energetically favorable configuration, while those in panels (a) and (c) lie 160 meV and 37 meV above, respectively. A similar trend is observed for 25-15 Type-II junctions, where the configuration in panel (f) is the lowest in energy. The second one is displayed in panel (e) at 23 meV, and the less favorable configuration is the geometry of panel (d) at 327 meV above the one in panel (f).

F. First excited magnetic state at the interface

We have shown in Sec. IV A that N_{int} depends on the number of bonds at the interface. In particular, for Type-I heterojunctions composed of AGNRs with the same topological character Z —and thus the same number of ESs— N_{int} can still be non zero when the ribbons are only partially connected. This is due to the presence of unhybridized ESs (see Fig. 2). It is natural then, to expect emerging localized spins at the interface when the number of C-C bonds between the AGNRs is reduced. To investigate the magnetic character of the unhybridized ESs in such junctions, we consider a 21-19 junction with a Type-I interface, that we have already characterized in absence of Coulomb repulsion interactions in Sec. IV A. In Fig. 5a we plot the GS for the case with one single C-C bond (results for the remaining 21-19 junctions can be found in Fig. S10 [53]). Here we can see that local magnetic moments develop at each side of the uncoupled parts at the junction area (red and blue areas). These local moments, labeled by S_z^ℓ and S_z^r for the left and right ribbons, are numerically calculated by summing the atomic spin polarizations over each AGNR: $S_z^{\ell,r} = \sum_i s_z(i)$ with $i \in \ell, r$, respectively. The color, red or blue, indicates respectively up or down spin projection. Notice that $S_z = S_z^\ell + S_z^r$. We observe that the magnetic GS of these junctions is $S_z = 0$, regardless the bonding configuration, in line with Eq. (9).

For the particular case of the 21-19 Type-I junction with one single bond at the interface, the local spin moments are $S_z^\ell = -S_z^r \approx 1$ [Fig. 5a], consistent with the presence of two unhybridized states in each AGNR [see Fig. 2d(i)]. This kind of behavior illustrates the general validity of Eq. (9). Within each AGNR, atomic spin moments $s_z(i)$ orient in a parallel disposition, as expected [28, 56]. This gives rise to two spin mo-

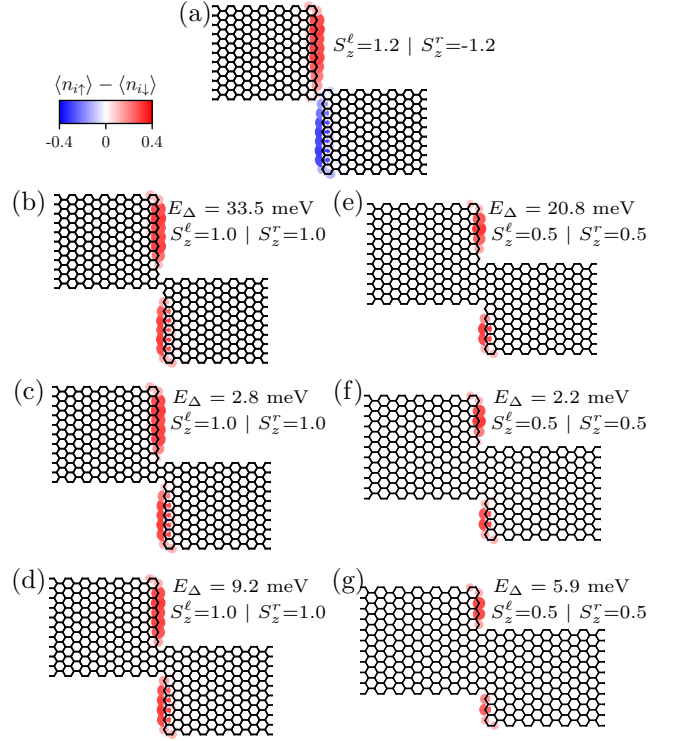


FIG. 5. Spin density distribution in partially joined 21-19 Type-I junctions. (a) GS of the junction with one bond at the interface. (b-g) First excited state for different vertical alignments (one to six bonds, respectively). The local spins S_z^ℓ and S_z^r , and the excitation energy E_Δ for each geometry are annotated in each panel. Size and color of the blobs at each site indicates both the magnitude and sign of the spin density, as indicated by the inset colorbar, common for all panels. These calculations were performed with open boundary conditions and $U = 3$ eV.

ments localized at each side of the junction with magnitude $|S_z^{\ell,r}| \approx \frac{1}{2} [M_{\ell,r} - \text{rank}(\mathcal{V})]$, corresponding to the number of unhybridized states in each AGNR. Across the interface, these moments couple antiferromagnetically, in line with the expected alignment between opposite sublattices [57], resulting in a total spin moment $|S_z| = |S_z^\ell - S_z^r| = \frac{1}{2} |M_\ell - M_r| = \frac{1}{2} N_{\text{int}}^{\text{full}}$.

Another very interesting aspect of these partially-coupled junctions is their first excited magnetic state, which depends sensitively on the number of unhybridized states. This first excited state corresponds to a parallel alignment of S_z^r and S_z^ℓ . Consequently, depending on the number of C-C bonds at the interface, the magnitude of the total spin of this excited state is determined by N_{int} ,

$$|S_z^{\text{exc}}| = \frac{1}{2} N_{\text{int}}. \quad (10)$$

In Fig. 5(b-g) we plot the spin density distribution of the first excited state for 21-19 Type-I heterojunctions of different bonding configurations. Here we see that, the first excited magnetic state of the junctions with one,

two, and three C-C bonds at the interface [panels (b-d)] corresponds to $S_z = 2$, since $S_z^{\ell,r} = 1$. This is consistent with the number of interface states $N_{\text{int}} = 4$ obtained from our analysis at $t_{\text{int}} = t$, for the cases with one and three bonds [see Fig. 2d(i-ii)]. Similarly, panels (e-g) display the excited states for junctions with four to six interfacial bonds, respectively. Here, $S_z^{\ell,r} = 0.5$ for the first excited state (*i.e.*, $S_z = 1$), in agreement with our finding of $N_{\text{int}} = 2$ for the case with five bonds seen in Fig. 2d(iii). Junctions with higher interfacial connectivity are not shown, as we have verified that geometries with 7 or more bonds exhibit no spin-polarized states. This agrees with the absence of zero-energy states found in these cases illustrated in Fig. 2c(iv-v).

We now turn our attention to the difference between the energy of the excited state (E_{S_z}) and that of the GS (E_0), $E_{\Delta} \equiv E_{S_z} - E_0$. This excitation energy shows a highly non-monotonic dependence with respect to the geometry of the heterojunction. For instance, in Fig. 5(b-d), the junctions with one, two and three bonds at the interface show $E_{\Delta} = 33.5, 2.8, 9.2$ meV, respectively. Similarly, for the junctions shown in panels (e-g), the excitation energy is $E_{\Delta} = 20.8, 2.2, 5.9$ meV for four, five and six C-C bonds at the interface, respectively.

Other AGNR width combinations included in the SM (Figs. S11-S14) [53], demonstrate that this behavior is not unique to the example discussed here. For the junctions with one C-C bond at the interface E_{Δ} lies in the range 30–40 meV. The case with two C-C bonds lies close to ~ 3 meV, and in the case with three C-C bonds lies more or less close to ~ 10 meV. The oscillatory behavior of E_{Δ} continues when the number of bonds is further increased. Notice that the total magnetic moment of the excited state changes abruptly by one (following a corresponding reduction of N_{int}) when the number of bonds is increased to four (up to six). Interestingly, this magnetic moment reduction is accompanied by an increase of the value of E_{Δ} , which might be considered an unintuitive behavior. The discussed non-trivial evolution of E_{Δ} applies to all the analyzed cases and may therefore represent a general feature of these junctions.

V. CONCLUSIONS

In summary, we have presented a detailed theoretical study of the interface states that appear in AGNR heterojunctions. By combining TB and MFH calculations, we have systematically analyzed the interplay between ribbon width, interface bonding, and geometric deformations in determining the number of localized interface states and their magnetic properties. In particular, we have expressed the number of interface states in terms of M_{ℓ} , M_r , and the number of hybridized states. In a perturbative treatment, this can be calculated as the rank of the coupling matrix in the subspace of ESs of the AGNRs, \mathcal{V} . For instance, for fully-coupled AGNRs, this relation boils down to $N_{\text{int}}^{\text{full}} = |M_{\ell} - M_r|$. Also, the two

types of junctions, Type-I and Type-II, are related by $N_{\text{int}}^{II} = |N_{\text{int}}^I - 1|$.

We also investigated the impact of uniaxial strain applied along the junction axis using a minimal model in which the hopping parameters are altered via a dimensionless parameter. This simplified approach revealed that strain can induce topological phase transitions in AGNRs. These transitions significantly alter the number of interface states, providing a controllable mechanism for engineering the electronic and magnetic properties of AGNR junctions. In fact, the interface magnetic moment is expected to vary with strain, in line with the strain dependence of N_{int} .

In addition, our analysis of the spin states at the junctions revealed a direct correlation between N_{int} and the resulting spin moment at the interface, S_z . Remarkably, the total spin moment of the GS at the interface turns out to be independent on the bonding configuration, $S_z^{\text{GS}} = \frac{1}{2}|M_{\ell} - M_r| = \frac{1}{2}N_{\text{int}}^{\text{full}}$. For partially-coupled ribbons, the magnetization distribution of the GS can be interpreted as the antiparallel alignment of two magnetic moments localized at each side of the junction, S_z^r and S_z^{ℓ} . The lowest-lying magnetic excited state for these partially-coupled Type-I junctions corresponds to a parallel alignment of S_z^r and S_z^{ℓ} , with total magnetic moment $S_z^{\text{exc}} = \frac{1}{2}N_{\text{int}}$. The energy of this magnetic excitation E_{Δ} shows a surprising non-monotonic dependence on the number of C-C bonds at the interface, which appears to be a general feature for Type-I junctions, *i.e.*, irrespective of the width combination, and somewhat difficult to reconcile with a Heisenberg model (*e.g.*, a decrease of both S_z^r and S_z^{ℓ} is accompanied by an increase on E_{Δ} when going from three to four bonds at the interface).

Our findings contribute to a deeper understanding of the electronic and magnetic properties of AGNR heterojunctions. By providing a set of predictive “rules of thumb”, this work offers a framework for designing AGNR-based devices with tunable electronic and magnetic properties. These insights pave the way for the development of nanoscale circuits and spintronic devices, leveraging the unique interplay of topology, geometry, and magnetism in GNR heterostructures.

ACKNOWLEDGEMENTS

This work was funded by the Spanish MCIN/AEI/10.13039/501100011033 (PID2022-140854OB-C66, and JDC2022-048665-I), the Basque Department of Education (PIBA-2020-1-0014), the University of the Basque Country (UPV/EHU) through Grant IT-1569-22.

Appendix A: DFT calculations

In this section, we present complementary DFT calculations for the magnetic states of 25-15 Type-I junc-

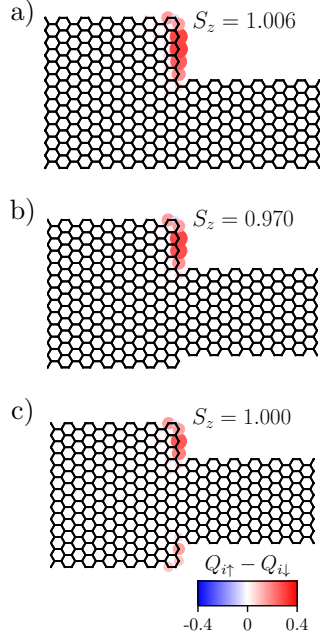


FIG. 6. Atom-resolved spin polarization calculated with SIESTA for three different vertical alignments of 25-15 Type-I junctions (a-c). The magnetic moment S_z at the interface is annotated in each panel. Inset colorbar is common to all panels.

tions. The simulations were performed using the SIESTA package [58], with the PBE-GGA exchange-correlation functional [59]. We used a double-zeta polarized (DZP) basis set, a mesh cutoff of 400 Ry, and an energy shift of 0.02 Ry to define the cutoff radii of the orbitals. All cal-

culations were carried out at an electronic temperature of $T = 100$ K. We modeled finite-length AGNR junctions comprising $L = 30$ unit cells for each AGNR (an approximate total length of 255 Å), which ensures negligible hybridization between spin-polarized states at the interface and those at the free ends of the ribbons. All dangling bonds were passivated with hydrogen atoms.

First, the geometries were relaxed in the non-spin-polarized configuration by fixing the carbon atoms and allowing hydrogen atoms to relax until the maximum residual force was below 0.02 eV/Å. The resulting geometries were then used in spin-polarized calculations, without further structural relaxation. Convergence for the electronic density matrix was set to 10^{-5} in all cases. Numerically, the total spin moment was evaluated from the Mulliken population difference between spin-up (Q_{\uparrow}) and spin-down (Q_{\downarrow}) components, $S_z = \frac{1}{2} \sum_i (Q_{i\uparrow} - Q_{i\downarrow})$. Since in this case we are dealing with finite junctions, the sum is restricted to atomic sites i with coordinates in the range $x_{\ell} \leq x_i \leq x_r$, where x_{ℓ} (x_r) denotes the x -coordinate of the center of the left (right) AGNR. This spatial window is chosen to account for the finite decay length of the ESs.

Fig. 6 shows the DFT-computed spin polarization resolved per atom for a 25-15 junction, for three different vertical alignments [panels (a-c)], in analogy with Fig. 4(a-c). The spin moment localized at the interface is annotated in each case. By comparing Fig. 6(a-c) with Fig. 4(a-c), and the resulting calculated spin moments, we conclude that the MFH model reproduces the more accurate DFT description. Note that the short distance between some of the hydrogen atoms at the interface gives rise to structural relaxations and other effects that are not captured at the MFH level, precluding a meaningful comparison of the total energies.

-
- [1] K. Nakada, M. Fujita, G. Dresselhaus, and M. S. Dresselhaus, Edge state in graphene ribbons: Nanometer size effect and edge shape dependence, *Phys. Rev. B* **54**, 17954 (1996).
 - [2] K. Wakabayashi, M. Fujita, H. Ajiki, and M. Sigrist, Electronic and magnetic properties of nanographite ribbons, *Phys. Rev. B* **59**, 8271 (1999).
 - [3] A. R. Rocha, V. M. García-suárez, S. W. Bailey, C. J. Lambert, J. Ferrer, and S. Sanvito, Towards molecular spintronics, *Nature Materials* **4**, 335 (2005).
 - [4] Y.-W. Son, M. L. Cohen, and S. G. Louie, Energy gaps in graphene nanoribbons, *Phys. Rev. Lett.* **97**, 216803 (2006).
 - [5] L. Brey and H. A. Fertig, Electronic states of graphene nanoribbons studied with the dirac equation, *Phys. Rev. B* **73**, 235411 (2006).
 - [6] Y.-W. Son, M. L. Cohen, and S. G. Louie, Half-metallic graphene nanoribbons, *Nature* **444**, 347 (2006).
 - [7] M. Y. Han, B. Özyilmaz, Y. Zhang, and P. Kim, Energy band-gap engineering of graphene nanoribbons, *Phys. Rev. Lett.* **98**, 206805 (2007).
 - [8] D. A. Areshkin and C. T. White, Building blocks for integrated graphene circuits, *Nano Lett.* **7**, 3253 (2007).
 - [9] L. Yang, C.-H. Park, Y.-W. Son, M. L. Cohen, and S. G. Louie, Quasiparticle energies and band gaps in graphene nanoribbons, *Phys. Rev. Lett.* **99**, 186801 (2007).
 - [10] S. M.-M. Dubois, Z. Zanolli, X. Declerck, and J.-C. Charlier, Electronic properties and quantum transport in graphene-based nanostructures, *The European Physical Journal B* **72**, 1 (2009).
 - [11] F. Schwierz, Graphene transistors, *Nat. Nanotechnol.* **5**, 487 (2010).
 - [12] W. Jaskólski, A. Ayuela, M. Pelc, H. Santos, and L. Chico, Edge states and flat bands in graphene nanoribbons with arbitrary geometries, *Phys. Rev. B* **83**, 235424 (2011).
 - [13] P. B. Bennett, Z. Pedramrazi, A. Madani, Y.-C. Chen, D. G. de Oteyza, C. Chen, F. R. Fischer, M. F. Crommie, and J. Bokor, Bottom-up graphene nanoribbon field-effect transistors, *Applied Physics Letters* **103**, 253114 (2013).
 - [14] A. W. Cummings, S. O. Valenzuela, F. Ortmann, and

- S. Roche, Graphene spintronics, in *2D Materials: Properties and Devices*, edited by P. Avouris, T. F. Heinz, and T. Low (Cambridge University Press, 2017) p. 197–218.
- [15] J. Zhang, L. Qian, G. B. Barin, A. H. S. Daaoub, P. Chen, K. Müllen, S. Sangtarash, P. Ruffieux, R. Fasel, H. Sadeghi, J. Zhang, M. Calame, and M. L. Perrin, Contacting individual graphene nanoribbons using carbon nanotube electrodes, *Nature Electronics* **6**, 572 (2023).
- [16] J. Cai, P. Ruffieux, R. Jaafar, M. Bieri, T. Braun, S. Blankenburg, M. Muoth, A. P. Seitsonen, M. Saleh, X. Feng, K. Müllen, and R. Fasel, Atomically precise bottom-up fabrication of graphene nanoribbons, *Nature* **466**, 470 (2010).
- [17] P. Ruffieux, S. Wang, B. Yang, C. Sánchez-Sánchez, J. Liu, T. Dienel, L. Talirz, P. Shinde, C. A. Pignedoli, D. Passerone, T. Dumschlaff, X. Feng, K. Müllen, and R. Fasel, On-surface synthesis of graphene nanoribbons with zigzag edge topology, *Nature* **531**, 489 (2016).
- [18] T. Cao, F. Zhao, and S. G. Louie, Topological phases in graphene nanoribbons: junction states, spin centers, and quantum spin chains, *Phys. Rev. Lett.* **119**, 076401 (2017).
- [19] O. Gröning, S. Wang, X. Yao, C. A. Pignedoli, G. Borin Barin, C. Daniels, A. Cupo, V. Meunier, X. Feng, A. Narita, K. Müllen, P. Ruffieux, and R. Fasel, Engineering of robust topological quantum phases in graphene nanoribbons, *Nature* **560**, 209 (2018).
- [20] D. J. Rizzo, G. Veber, T. Cao, C. Bronner, T. Chen, F. Zhao, H. Rodriguez, S. G. Louie, M. F. Crommie, and F. R. Fischer, Topological band engineering of graphene nanoribbons, *Nature* **560**, 204 (2018).
- [21] J. Jiang and S. G. Louie, Topology classification using chiral symmetry and spin correlations in graphene nanoribbons, *Nano Lett.* **21**, 197 (2021).
- [22] M. P. López-Sancho and M. C. Muñoz, Topologically protected edge and confined states in finite armchair graphene nanoribbons and their junctions, *Phys. Rev. B* **104**, 245402 (2021).
- [23] A. D. Zdetsis and E. Economou, Topological metal-insulator transition in narrow graphene nanoribbons?, *Carbon* **176**, 548 (2021).
- [24] J. Li, S. Sanz, N. Merino-Díez, M. Vilas-Varela, A. Garcia-Lekue, M. Corso, D. G. de Oteyza, T. Frederiksen, D. Peña, and J. I. Pascual, Topological phase transition in chiral graphene nanoribbons: from edge bands to end states, *Nat. Commun.* **12**, 5538 (2021).
- [25] A. D. Zdetsis, Peculiar electronic properties of wider armchair graphene nanoribbons: Multiple topological end-states and “phase transitions”, *Carbon* **210**, 118042 (2023).
- [26] L. Fu and C. L. Kane, Topological insulators with inversion symmetry, *Phys. Rev. B* **76**, 045302 (2007).
- [27] J. Zak, Berry’s phase for energy bands in solids, *Phys. Rev. Lett.* **62**, 2747 (1989).
- [28] A. D. Zdetsis, Do we really understand graphene nanoribbons? a new understanding of the $3n$, $3n \pm 1$ rule, edge “magnetism”, and much more, *J. Phys. Chem. C* **124**, 7578 (2020).
- [29] J. Lawrence, P. Brandimarte, A. Berdonces-Layunta, M. S. G. Mohammed, A. Grewal, C. C. Leon, D. Sánchez-Portal, and D. G. de Oteyza, Probing the magnetism of topological end states in 5-armchair graphene nanoribbons, *ACS Nano* **14**, 4499 (2020).
- [30] A. García-Fuente, D. Carrascal, G. Ross, and J. Ferrer, Full analytical solution of finite-length armchair/zigzag nanoribbons, *Phys. Rev. B* **107**, 115403 (2023).
- [31] H. Sevinçli, M. Topsakal, and S. Ciraci, Superlattice structures of graphene-based armchair nanoribbons, *Phys. Rev. B* **78**, 245402 (2008).
- [32] J. Cai, C. A. Pignedoli, L. Talirz, P. Ruffieux, H. Söde, L. Liang, V. Meunier, R. Berger, R. Li, X. Feng, K. Müllen, and R. Fasel, Graphene nanoribbon heterojunctions, *Nat. Nanotechnol.* **9**, 896 (2014).
- [33] Y.-C. Chen, T. Cao, C. Chen, Z. Pedramrazi, D. Haberer, D. G. de Oteyza, F. R. Fischer, S. G. Louie, and M. F. Crommie, Molecular bandgap engineering of bottom-up synthesized graphene nanoribbon heterojunctions, *Nature Nanotechnology* **10**, 156 (2015).
- [34] S. Wang, N. Kharche, E. Costa Girão, X. Feng, K. Müllen, V. Meunier, R. Fasel, and P. Ruffieux, Quantum dots in graphene nanoribbons, *Nano Lett.* **17**, 4277 (2017).
- [35] Y.-L. Lee, F. Zhao, T. Cao, J. Ihm, and S. G. Louie, Topological phases in cove-edged and chevron graphene nanoribbons: Geometric structures, z_2 invariants, and junction states, *Nano Lett.* **18**, 7247 (2018).
- [36] K.-S. Lin and M.-Y. Chou, Topological properties of gapped graphene nanoribbons with spatial symmetries, *Nano Letters*, *Nano Lett.* , (2018).
- [37] J.-P. Joost, A.-P. Jauho, and M. Bonitz, Correlated topological states in graphene nanoribbon heterostructures, *Nano Lett.* **19**, 9045 (2019).
- [38] D. J. Rizzo, G. Veber, J. Jiang, R. McCurdy, T. Cao, C. Bronner, T. Chen, S. G. Louie, F. R. Fischer, and M. F. Crommie, Inducing metallicity in graphene nanoribbons via zero-mode superlattices, *Science* **369**, 1597 (2020).
- [39] G. Tamaki, T. Kawakami, and M. Koshino, Topological junction states and their crystalline network in systems with chiral symmetry: Application to graphene nanoribbons, *Phys. Rev. B* **101**, 205311 (2020).
- [40] J. Ostmeier, L. Razmadze, E. Berkowitz, T. Luu, and U.-G. Meißner, Effective theory for graphene nanoribbons with junctions, *Phys. Rev. B* **109**, 195135 (2024).
- [41] Y. Lv, Q. Huang, S. Chang, H. Wang, J. He, C. Wei, A. Liu, S. Ye, and W. Wang, Interface coupling as a crucial factor for spatial localization of electronic states in a heterojunction of graphene nanoribbons, *Phys. Rev. Appl.* **11**, 024026 (2019).
- [42] H. Santos, A. Latgé, L. Brey, and L. Chico, Spin-polarized currents in corrugated graphene nanoribbons, *Carbon* **168**, 1 (2020).
- [43] J. Hubbard, Electron correlations in narrow energy bands, *Proc. R. Soc. A* **276**, 238 (1963).
- [44] J. Fernández-Rossier and J. J. Palacios, Magnetism in graphene nanoislands, *Phys. Rev. Lett.* **99**, 177204 (2007).
- [45] O. V. Yazyev, Emergence of magnetism in graphene materials and nanostructures, *Rep. Prog. Phys.* **73**, 056501 (2010).
- [46] Y. Hancock, A. Uppstu, K. Saloriotta, A. Harju, and M. J. Puska, Generalized tight-binding transport model for graphene nanoribbon-based systems, *Phys. Rev. B* **81**, 245402 (2010).
- [47] J. Li, S. Sanz, M. Corso, D. J. Choi, D. Peña, T. Frederiksen, and J. I. Pascual, Single spin localization and manipulation in graphene open-shell nanostructures, *Nat. Commun.* **10**, 200 (2019).

- [48] A. H. Castro Neto, F. Guinea, N. M. R. Peres, K. S. Novoselov, and A. K. Geim, The electronic properties of graphene, *Rev. Mod. Phys.* **81**, 109 (2009).
- [49] S. Sanz, N. Papior, M. Brandbyge, and T. Frederiksen, *hubbard: v0.4.2* (2024).
- [50] N. Papior, *sisl: v0.15.0* (2025).
- [51] S. Sanz, N. Papior, G. Giedke, D. Sánchez-Portal, M. Brandbyge, and T. Frederiksen, Spin-polarizing electron beam splitter from crossed graphene nanoribbons, *Phys. Rev. Lett.* **129**, 037701 (2022).
- [52] W. P. Su, J. R. Schrieffer, and A. J. Heeger, Solitons in polyacetylene, *Phys. Rev. Lett.* **42**, 1698 (1979).
- [53] See Supplemental Material for details on methodology and additional calculations,.
- [54] A. Kimouche, M. M. Ervasti, R. Drost, S. Halonen, A. Harju, P. M. Joensuu, J. Sainio, and P. Liljeroth, Ultra-narrow metallic armchair graphene nanoribbons, *Nature Communications* **6**, 10177 (2015).
- [55] H. Zhang, H. Lin, K. Sun, L. Chen, Y. Zaganyarski, N. Aghdassi, S. Duhm, Q. Li, D. Zhong, Y. Li, K. Müllen, H. Fuchs, and L. Chi, On-surface synthesis of rylene-type graphene nanoribbons, *J. Am. Chem. Soc.* **137**, 4022 (2015).
- [56] A. García-Fuente and J. Ferrer, Solution of the mean-field hubbard model of graphene rectangulenes (2024), [arXiv:2405.04085 \[cond-mat.str-el\]](https://arxiv.org/abs/2405.04085).
- [57] E. H. Lieb, Two theorems on the hubbard model, *Phys. Rev. Lett.* **62**, 1201 (1989).
- [58] J. M. Soler, E. Artacho, J. D. Gale, A. García, J. Junquera, P. Ordejón, and D. Sánchez-Portal, The siesta method for ab initio order- n materials simulation, *J. Phys.: Condens. Matter* **14**, 2745 (2002).
- [59] J. P. Perdew, K. Burke, and M. Ernzerhof, Generalized gradient approximation made simple, *Phys. Rev. Lett.* **77**, 3865 (1996).

Supplementary information: Predicting interface and spin states in armchair graphene nanoribbon junctions

Sofia Sanz^{1,*} and Daniel Sánchez-Portal^{1,†}

¹*Centro de Física de Materiales (CFM) CSIC-
UPV/EHU, E-20018, Donostia-San Sebastián, Spain*

CONTENTS

S1. Topological bands and end-state counting in AGNRs	2
S2. Calculation of N_{int} and LDOS	6
S3. Systematic calculation of N_{int} for multiple width combinations	8
S4. Comparison between effective model and full TB Hamiltonian	9
S5. Rank of \mathcal{V} for two case examples	10
S6. Spin polarization for partially joined 25-15 junctions	12
S7. Magnetic ground state of the 21-19 junctions	14
S8. E_{Δ} for other width combinations	15
References	16

* sofia.sanzwuhl@ehu.eus

† daniel.sanchez@ehu.eus

S1. TOPOLOGICAL BANDS AND END-STATE COUNTING IN AGNRS

The 1NN π -TB provides a simple way to understand the electronic properties of graphene. Using a rectangular supercell containing four atoms, as depicted in Fig. S1a, and applying periodic boundary conditions along the zigzag direction, the 2D problem gets mapped into a collection of disjoint 1D systems, as sketched in Fig. S1b. These 1D systems show two alternating hopping parameters, one of which depends explicitly on the Bloch vector along the zigzag direction $t'(k_Z)$, while the other maintains the original value t , yielding an SSH-like model. Cutting graphene along the zigzag edge effectively breaks bonds between sites 1 and 2, or equivalently between sites 3 and 4. In either case, according to the well-known physics of the SSH model, we can expect the appearance of an edge state whenever the condition

$$t > t'(k_Z) = 2t \cos(k_Z \frac{a}{2}) \quad (\text{S1})$$

is fulfilled. The graphene lattice parameter a is defined in Fig. S1a. Note that the SSH-chains in this formulation can be described with a unit-cell containing two effective atoms, highlighting the equivalence between atom pairs (1,2) and (3,4) in graphene.

By imposing confinement along the zigzag direction (Fig. S1a), as highlighted in blue in Fig. S2, the graphene continuum band structure becomes quantized into discrete transverse modes (k_n) that form the AGNR band structure [1]. These boundary conditions lead to the

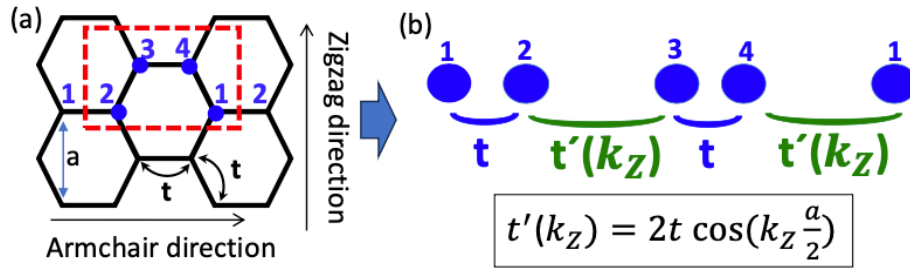


FIG. S1. (a) Rectangular graphene supercell containing four atoms with the axes oriented along the armchair (horizontal) and zigzag (vertical) directions. Red dashed lines delimitate the rectangular unit-cell. (b) Mapping of the graphene rectangular unit cell onto an SSH-like chain with two alternating hopping parameters $t'(k_z)$ and t .

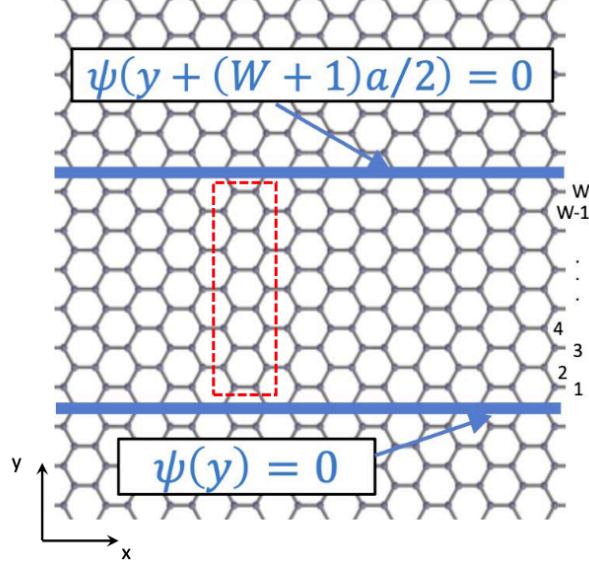


FIG. S2. Sketch of the real-space quantization conditions that must be imposed to a graphene layer to obtain the W -AGNR wave function $\psi(y)$. The W -AGNR unit cell is represented by the red rectangle.

following allowed transverse modes [2]:

$$k_n = \frac{2\pi n}{(W+1)a}, \text{ with } n = 1, 2, \dots, \lfloor \frac{(W+1)}{2} \rfloor, \quad (\text{S2})$$

with $\lfloor x \rfloor$ the floor function.

The AGNR band structure can be thus described by a set of uncoupled SSH-chains with hopping parameters given by an intra-cell hopping $t_{\text{intra}} = 2t\cos(k_n \frac{a}{2})$ and an inter-cell hopping $t_{\text{inter}} = t$. Note that this procedure reproduces exactly the ribbon's band structure within a 1NN π -TB description. Accordingly, the AGNR bands can be classified by their k_n , which determines the number of nodes across the ribbon and its topological character. For instance, the topologically non-trivial bands appear for those k_n that fulfill Eq. (S1), *i.e.*, $t > 2t\cos(k_n \frac{a}{2})$. The global topological index Z of the AGNR is determined by the number of transverse modes that fulfill this condition.

Equation Eq. (S1) implies that an ES appears whenever the quantized transverse momentum satisfies $k_n > \frac{2\pi}{3a}$ or, alternatively, $n > \frac{W+1}{3}$. As a result, the number of ESs for a W -AGNR is given by:

$$M = \lfloor \frac{(W+1)}{2} \rfloor - \lfloor \frac{(W+1)}{3} \rfloor. \quad (\text{S3})$$

This equation is in fact correct for even values of W . However, for odd values of W , two

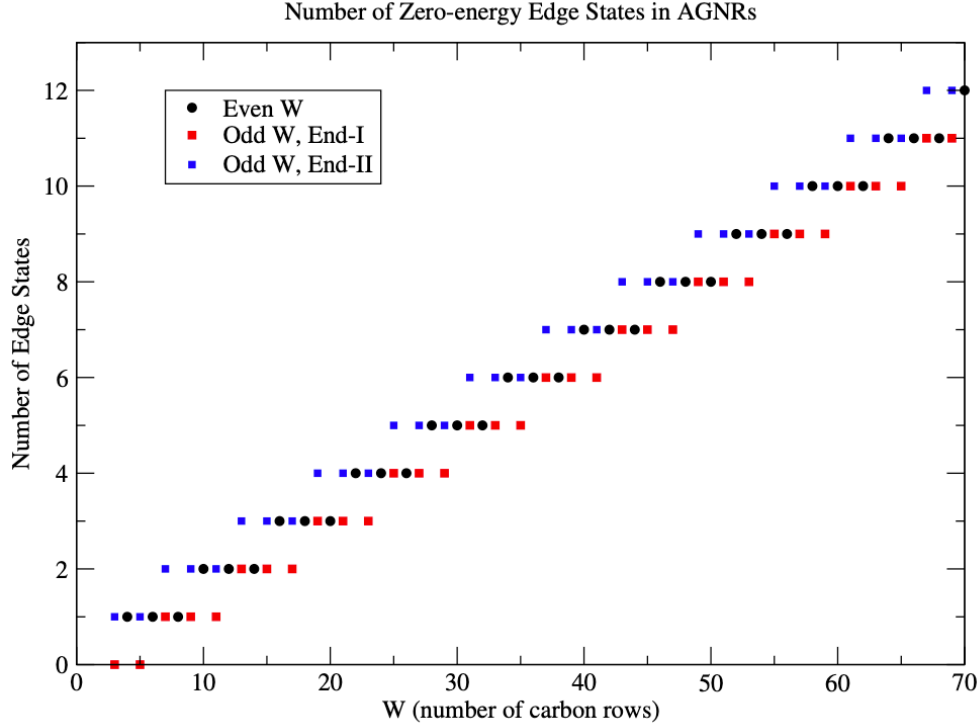


FIG. S3. Number of edge states as a function of the width W of a W -AGNR according to Eq. (S3). Results for even W are shown in black circles. Odd W with End-I and End-II (see Fig. 1) are shown in red and blue squares, respectively.

distinct terminations (End-I and End-II) are possible. These two terminations are not equivalent and affect the contribution of certain modes to the ESs count. In particular, $k_{(W+1)/2} = \pi/a$, which appears only for odd W , is spatially localized on the wider regions of the ribbon. This mode contributes with an ES only for an End-II termination. Therefore, for odd W , Eq. (S3) remains valid for End-II terminations, while for End-I the number of ESs is reduced by one, yielding $M_I = M - 1$. Note that AGNRs with $W = 3p + 2$, with p an integer, are metallic within the 1NN TB model. Therefore, Eq. (S3) is ambiguous for this class of AGNRs, as they are right at a topological transition point. Small changes in the relative sizes of the hopping parameters can thus change the number of ESs given in Eq. (S3) [3], as shown in Sec. IV D.

Following the same procedure used for graphene, a more detailed description of how a W -AGNR maps onto a set of decoupled SSH chains is sketched in Fig. S4. Here, the AGNR unit cell [panel (a)] is divided into blocks indexed by $i = \{1, 2, 3, 4\}$, each containing atoms

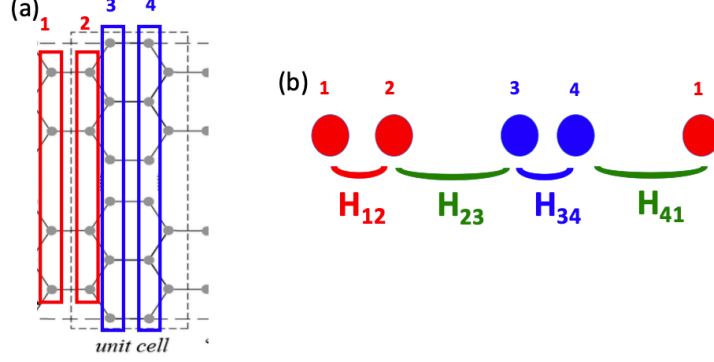


FIG. S4. (a) Mapping of the AGNR in blocks along the x -axis. (b) Sketch of the resulting effective 1D SSH-like chain formed by the AGNR transverse modes within each block.

located at the same x_i position. The transverse modes within each i th block are defined as:

$$\phi_i(k_n) = \mathcal{N}_n \sum_y \sin(k_n y) p_z(i, y), \quad (\text{S4})$$

where $p_z(i, y)$ is the p_z atomic orbital located at x_i and vertical position y . $\mathcal{N}_n = \frac{2}{\sqrt{W+1}}$ is a normalization factor for the n th mode, except for $k_n = \pi/a$, for which $\mathcal{N}_n = \sqrt{\frac{2}{W+1}}$. Note that $y=ma$ with $m = \{1, 2, \dots, \frac{W-1}{2}\}$ for blocks 1 and 2, and $y = \frac{(2m+1)}{2}a$ with $m = \{0, 1, 2, \dots, \frac{W-1}{2}\}$ for blocks 3 and 4, since blocks 1 and 2 contain $\frac{W-1}{2}$ atoms and blocks 3 and 4 contain $\frac{W+1}{2}$ atoms, respectively. As a consequence, modes $\phi_i(k_n = \frac{\pi}{a})$ for $i = \{1, 2\}$ vanish, and the SSH-like chains become a collection of disconnected (3,4) dimers giving rise to non-dispersive bands for that particular k_n . Since the wave function associated to this k_n is localized in the dimers (3,4), this band contributes with an additional ES only for the End-II termination. Expressing the 1NN TB Hamiltonian in the basis of transverse modes, $H_{ij}(k_n) = \langle \phi_i(k_n) | \hat{H} | \phi_j(k_n) \rangle$, we find $H_{12}(k_n) = H_{34}(k_n) = t$, while $H_{23}(k_n) = H_{41}(k_n) = 2t \cos(k_n \frac{a}{2})$, as expected from our previous discussion.

The uniaxial deformation along the x -axis considered in Sec. IV D modifies only the hopping amplitudes along bonds parallel to that direction, such that $t' = t(1 + \delta)$. In the transverse-mode basis, this translates into $H_{12}(k_n) = H_{34}(k_n) = t' = t(1 + \delta)$, while $H_{23}(k_n) = H_{41}(k_n) = 2t \cos(k_n \frac{a}{2})$. This modified hopping implies that the condition for the band to be topological [Eq. (S1)] now reads:

$$t' > 2t \cos(k_n \frac{a}{2}) \quad (\text{S5})$$

S2. CALCULATION OF N_{int} AND LDOS

To evaluate the number of interface-localized states, N_{int} , we first compute the projected density of states per atomic orbitals $p_z(i)$,

$$\text{PDOS}(E, i) = \sum_{\alpha} \frac{1}{\pi} \frac{\eta_E}{(E - E_{\alpha})^2 + \eta_E^2} |\phi_{\alpha}(i)|^2, \quad (\text{S6})$$

where $\phi_{\alpha}(i)$ is the α th eigenstate coefficient of the junction Hamiltonian at the atomic site i with coordinates (x_i, y_i) , and $\eta_E = 0.5$ meV is the broadening parameter. We then sum over the sites i around the interface and integrate over an energy window $\{-\delta E, \delta E\}$,

$$N_{\text{int}} = \int_{-\delta E}^{\delta E} \sum_i \text{PDOS}(E, i) dE, \quad (\text{S7})$$

such that the spectral weight of each state remains well-contained within the chosen energy window, while ensuring that the states remain inside the band-gap. For the case of the 21-19 junction (Fig. 2), the band gap energy is $E_g \sim 440$ meV, for which we use $\delta E = 50$ meV, enabling an accurate count of the modes that lie well-within the gap. Furthermore, this energy scale of ~ 100 meV is comparable with the typical splittings induced by the spin polarization in the $U = 3$ eV calculations, allowing for a better correlation between the computed values of the spin moments S_z and N_{int} . Note that the choice of parameters becomes of relative importance for the cases with an intermediate number of C-C bonds at the interface, since the hybridization of states evolves relatively slowly with t_{int} . For the extreme cases with one C-C bonds or maximum number of C-C bonds, N_{int} does not show dependence on small variations of this numerical choice.

The sum of the PDOS in Eq. (S7) runs over the atomic sites i such that $x_{\ell} \leq x_i \leq x_r$, where x_{ℓ} (x_r) is the x -coordinate of the center of the left (right) AGNR. We use these limits to account for the decay lengths of the ESs.

To calculate the LDOS map at x_{int} for an energy window, we also use a spatial distribution function along x ,

$$\text{LDOS}(E, x) = \sum_i \frac{1}{\eta_x \sqrt{2\pi}} \exp\left(\frac{-(x - x_i)^2}{2\eta_x^2}\right) \text{PDOS}(E, i), \quad (\text{S8})$$

with a broadening of $\eta_x = 0.5$ Å.

Since x_{int} lies in between atomic positions, we compute the $\text{LDOS}(E, x_{\text{int}})$ as,

$$\text{LDOS}(E, x_{\text{int}}) = \text{LDOS}(E, x_{\text{int}} - \frac{b}{2}) + \text{LDOS}(E, x_{\text{int}} + \frac{b}{2}). \quad (\text{S9})$$

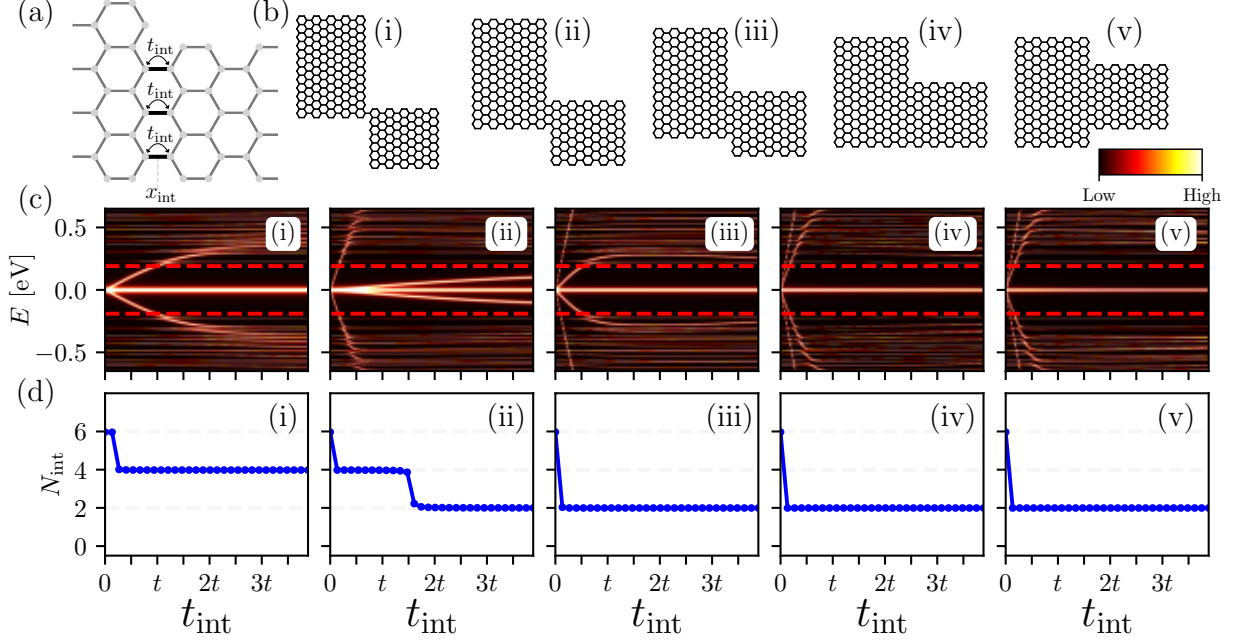


FIG. S5. Equivalent analysis of Fig. 2 for a 25-15 junction. Geometries (i-iv) have one to seven bonds at the interface in steps of two, respectively. Geometry (v) has also seven bonds but with a different vertical alignment than geometry (iv). Red dashed lines in panels (c), placed at $\pm E_g/2$, with $E_g = 381$ meV, delimitate the band gap for the 25-15 junction. These calculations were performed with $U = 0$.

Here $b = 1.42$ Å is the bond length between carbon atoms. In this way we sum the contribution from both AGNR ends at the interface. Both N_{int} and $\text{LDOS}(E, x_{\text{int}})$ were evaluated for each t_{int} to produce Fig. 2.

In Fig. S5 we plot an equivalent analysis of Fig. 2 for a 25-15 junction. Here we see that in this case the junction with maximum number of bonds [geometries (iv-v)] shows $N_{\text{int}} = 2$ in Fig. S5d(iv-v). We also observe that these two panels, corresponding to fully-coupled geometries but with different relative alignments, are almost indistinguishable by the eye.

S3. SYSTEMATIC CALCULATION OF N_{int} FOR MULTIPLE WIDTH COMBINATIONS

In Fig. S6 we show the calculated N_{int} for fully joined Type-I junctions for the width combinations of table I, as a function of the coupling strength t_{int} . In other words, we show graphically the results shown in this table. As it can be seen, the number of interface states as a function of t_{int} is in agreement with the results provided in table I for $t_{\text{int}} > 0$.

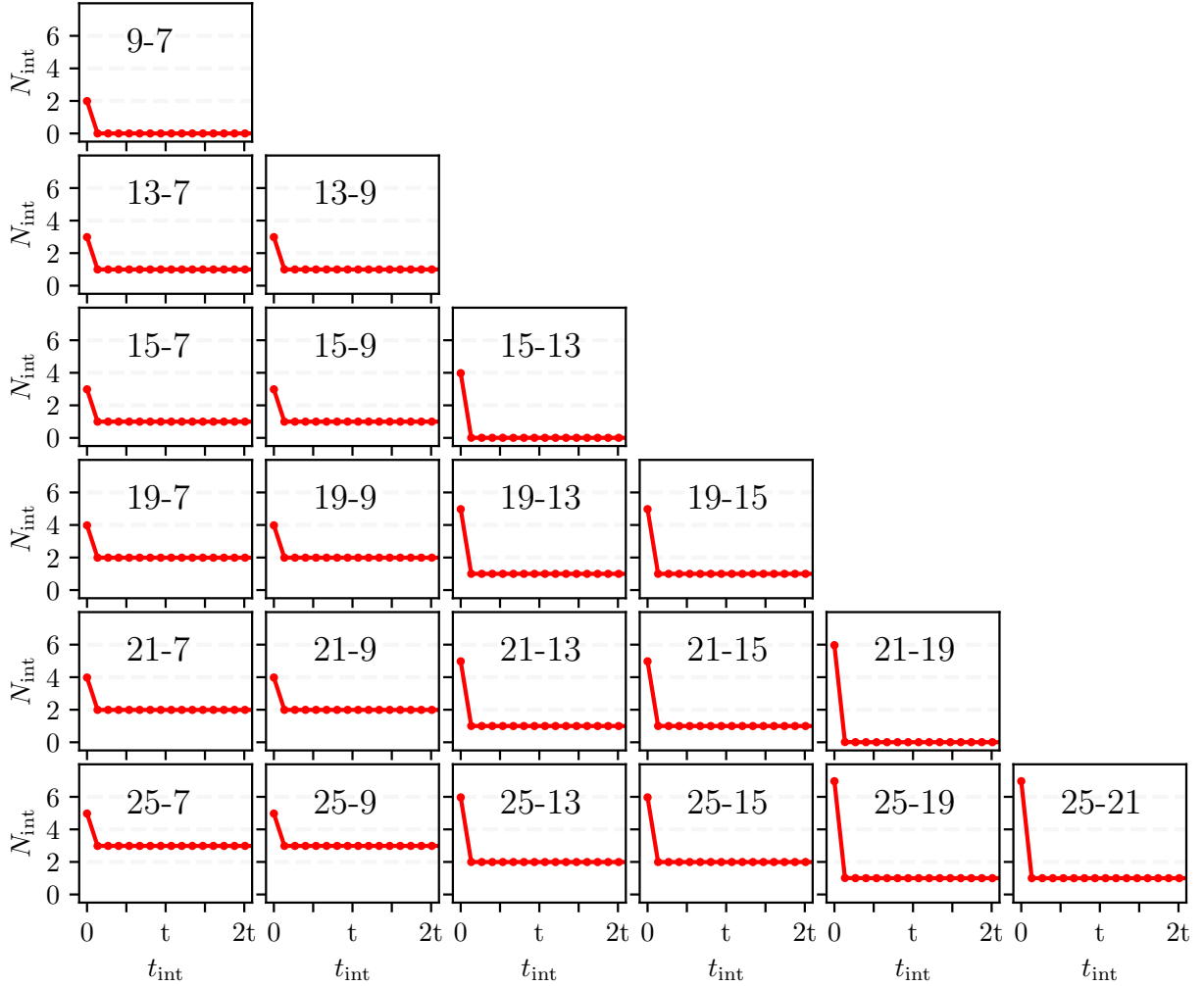


FIG. S6. Number of interface states, N_{int} , as a function of t_{int} , for different width combinations indicated in each panel. For all the heterojunctions considered here the number of C-C bonds at the interface is the maximum number allowed (fully joined AGNRs).

S4. COMPARISON BETWEEN EFFECTIVE MODEL AND FULL TB HAMILTONIAN

In Fig. S7, we compare the full tight-binding (TB) spectrum of the 21–19 junction for different vertical alignments [panels (a–e)] with that of the effective low-energy Hamiltonian of Eq. (4) shown in the main text. The excellent agreement between the full TB spectrum and the spectrum of H_{eff} confirms that the interaction between ESs is well described by this effective treatment, at least for the states lying within the gap (indicated by gray dashed lines in all panels), and away the strong coupling regime (*i.e.*, $t_{\text{int}} \lesssim t$). Note that, since we are dealing here with finite heterojunctions, panels (a–e) show states at $E = 0$, as the low energy spectrum contains ESs localized at the other ends of the ribbons.

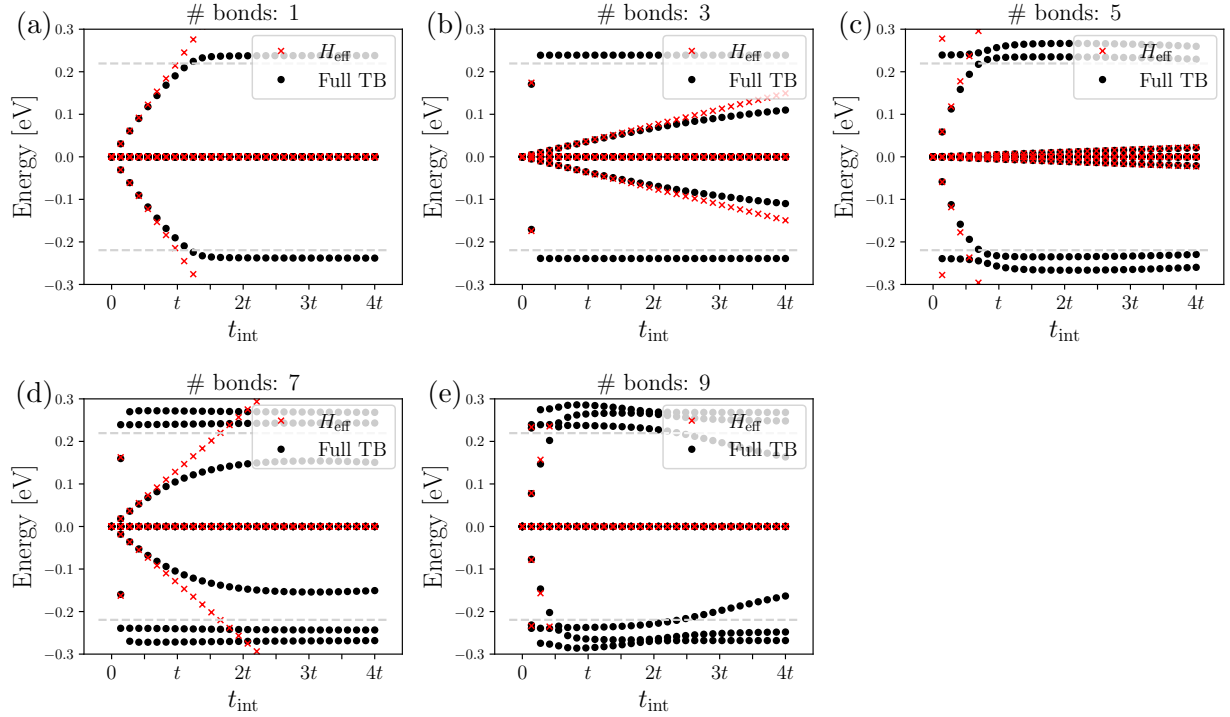


FIG. S7. Comparison of the low energy spectrum calculated from the Hamiltonian diagonalization (black dots) and with the effective Hamiltonian H_{eff} (red crosses) for the 21-19 junction as a function of t_{int} . Panels (a–e) show results for one to nine bonds at the interface, in steps of two, respectively. These calculations were performed with $U = 0$.

S5. RANK OF \mathcal{V} FOR TWO CASE EXAMPLES

In Fig. S8 we plot the rank of \mathcal{V} as a function of t_{int} and interface bonding configuration for four case examples: 21-19 Type-I junction (Fig. S8a), 21-19 Type-II junction (Fig. S8b), 21-15 Type-I junction (Fig. S8c), and 21-15 Type-II junction (Fig. S8d). We consider a tolerance of $\text{tol} = \delta E = 50$ meV to calculate the rank of this matrix in order to be consistent with our calculation of N_{int} (see Sec. S2).

In first place, by comparing Fig. 2 of the main text and Fig. S8a, we can clearly see that

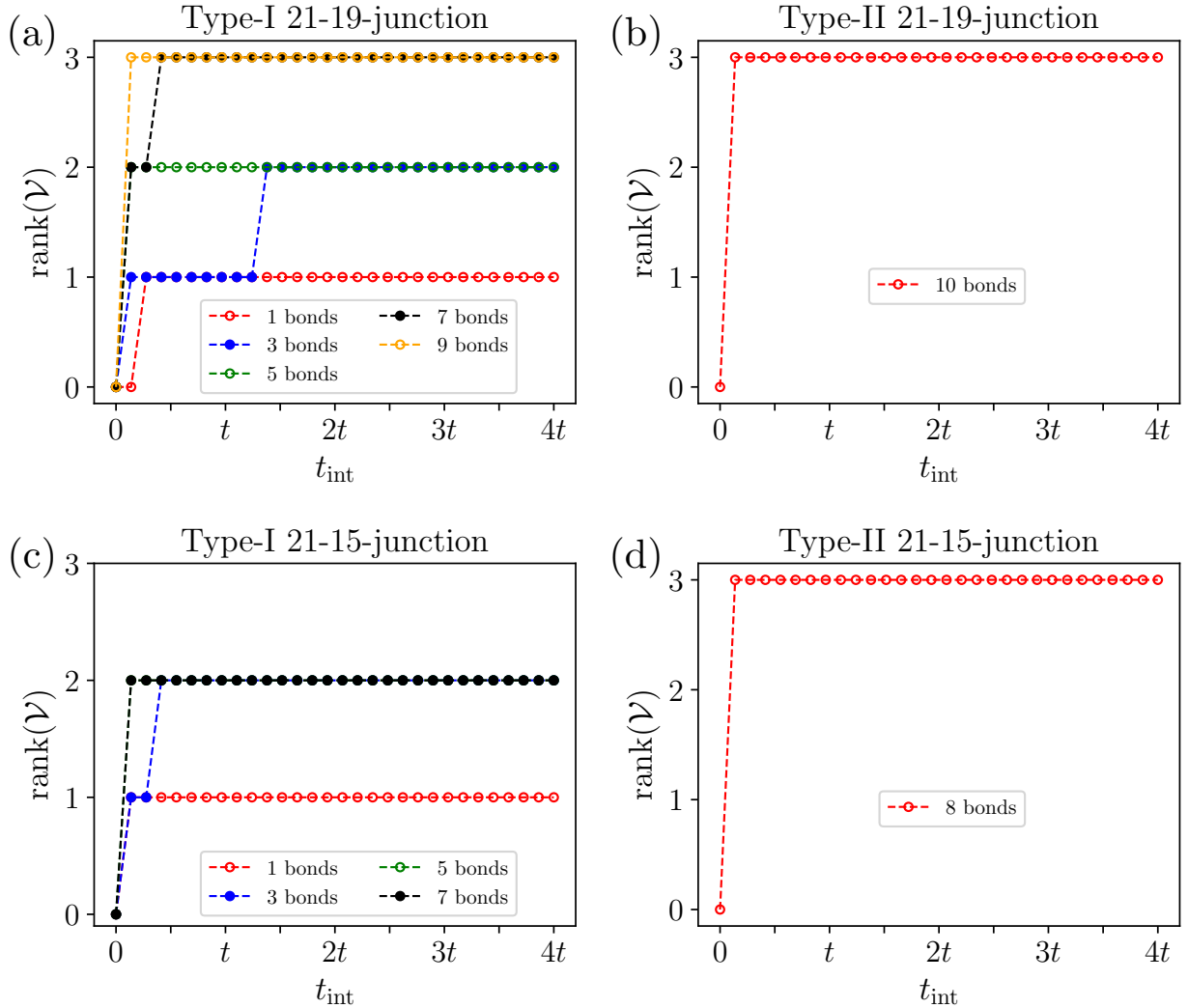


FIG. S8. Rank of the matrix \mathcal{V} for a (a) 21-19 Type-I junction, (b) 21-19 Type-II junction, (c) 21-15 Type-I junction and (d) 21-15 Type-II junction, calculated for different number of C-C bonds at the junctions (as indicated in each panel's legend). These calculations were performed with $U = 0$.

the rank of the coupling matrix for each t_{int} in the subspace of ESs of each AGNR explains the number of interface states for the different vertical alignments and coupling strengths.

In second place, by comparing panels Fig. S8a and Fig. S8b, we observe that $\text{rank}(\mathcal{V}_{II}) = \text{rank}(\mathcal{V}_I)$ for fully coupled 21-19 junctions (maximum number of bonds). In this case, this occurs because $M_\ell = M_r$, and therefore, the rank of this matrix is upper-limited by $\min(M_\ell, M_r)$, which in this case is the number of ESs of the End-I unit-cell (*i.e.*, M_ℓ). However, by comparing panel Fig. S8c and Fig. S8d, we observe that $\text{rank}(\mathcal{V}_{II}) = \text{rank}(\mathcal{V}_I) + 1$ for the fully coupled 21-15 junction, as in this case $M_\ell > M_r$.

S6. SPIN POLARIZATION FOR PARTIALLY JOINED 25-15 JUNCTIONS

Here we show the spin polarization of the magnetic GS of partially joined 25-15 Type-I junctions. In Fig. S9 we plot the spin density distribution at the junction with one to six bonds at the interface in panels (a-f), respectively. We also indicate the local spins S_z^ℓ and S_z^r , and the total energy E compared to the junction of lowest energy shown in the main text (Fig. 4b). Note that the total spin $S_z = S_z^\ell + S_z^r$. As it can be seen, the total spin moment at the interface is the same ($S_z = 1$) regardless the number of bonds at the interface. Note the correlation between the calculated N_{int} in Fig. S5 for $U = 0$ and the total spin moment S_z for the different number of C-C bonds at the interface shown in Fig. S9 for $U = 3$ eV. The local spins $S_z^{\ell,r}$ calculated for each geometry shown in Fig. S9 corroborate the approximate expressions of the main text that relate these spin moments with the ESs of each AGNR, *i.e.*, $S_z^{\ell,r} \approx \frac{1}{2}|M_{\ell,r} - \text{rank}(\mathcal{V})|$.

Focusing on the total energy we observe that, the less number of bonds at the interface leads to higher energy, as the junction gains energy by creating more bonds, as expected.

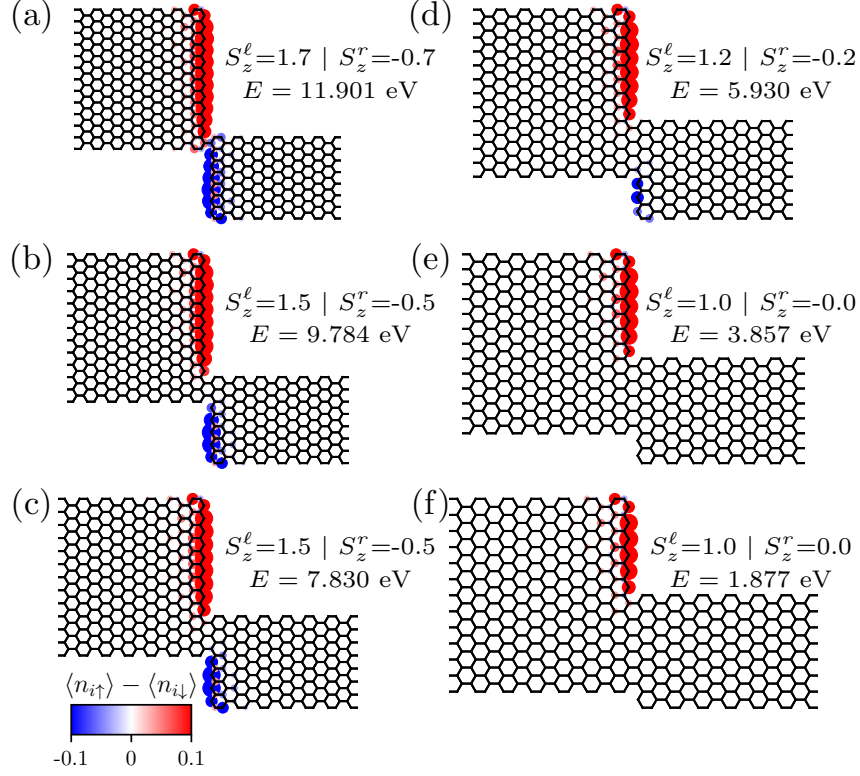


FIG. S9. Spin density distribution for the magnetic GS of the remaining partially joined 25-15 Type.I heterojunctions. The local spin moments $S_z^{\ell,r}$ are indicated in each panel. Panels (1-f) show junctions with one to six C-C bonds at the interface, respectively. Size and color of the blobs at each site show both the magnitude and sign of the spin polarization, as indicated by the inset colorbar, common for all panels. These calculations were performed with $U = 3$ eV and open boundary conditions.

S7. MAGNETIC GROUND STATE OF THE 21-19 JUNCTIONS

In Fig. 5 of the main text we show the first excited state for the 21-19 partially-joined junctions. In Fig. S10 we show the magnetic GS of the same junctions in panels (a-f). We observe that, regardless the number of C-C bonds at the interface the ground state is always represented by the magnetic state with $S_z = S_z^\ell + S_z^r = 0$.

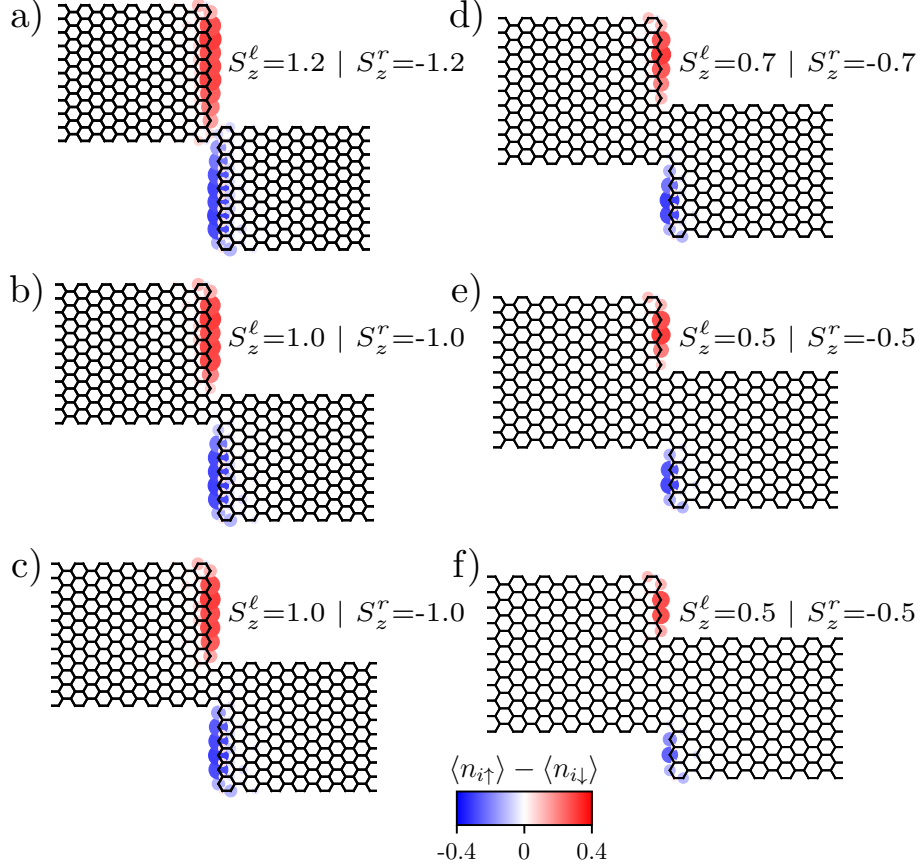


FIG. S10. Spin density distribution of the magnetic GS of the 21-19 AGNR junction for different vertical alignments (a-f). The local spin moments $S_z^{\ell,r}$ are annotated in each panel. Size and color of the blobs at each site shows both the magnitude and sign of the spin polarization, as indicated by the inset colorbar, common for all panels. These calculations were performed with $U = 3$ eV and open boundary conditions.

S8. E_Δ FOR OTHER WIDTH COMBINATIONS

In the main text we presented the first excited states for 21-19 Type-I partially-coupled junctions. Here we show a similar analysis for other width combinations. As in the main text, we focus on Type-I partially-coupled junctions. We compute the first excited states and the excitation energy E_Δ , for 19-15 junctions in Fig. S11, for 21-15 junctions in Fig. S12, for 25-19 junctions in Fig. S13, and in Fig. S14 for 25-21 junctions. Surprisingly, the non-monotonic growth of E_Δ with the number of bonds is not particular on the specific width combination, and persists across other junctions as well.

Again, the local spins $S_z^{\ell,r}$ calculated for each geometry shown in Figs. S11-S14 corroborate the approximate expressions of the main text $S_z^{\ell,r} \approx \frac{1}{2}|M_{\ell,r} - \text{rank}(\mathcal{V})|$.

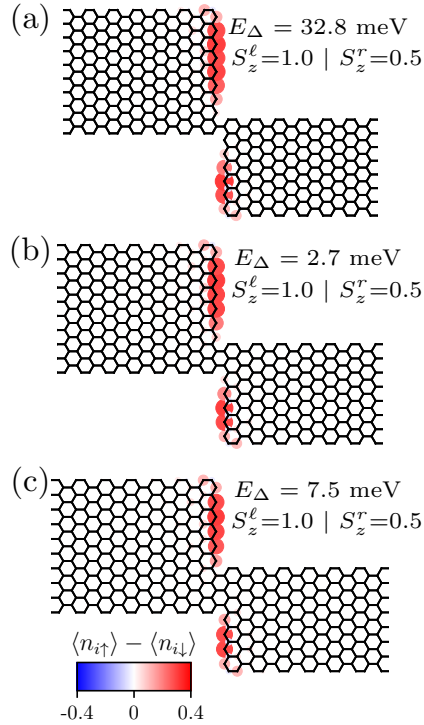


FIG. S11. Spin density distribution for the first excited state of a 19-15 heterojunction. The local spin moments $S_z^{\ell,r}$ and E_Δ are annotated in each panel. (a-c) Results for the junctions with one to three C-C bonds at the interface, respectively. Size and color of the blobs at each site shows both the magnitude and sign of the spin polarization, as indicated by the inset colorbar, common for all panels. These calculations were performed with $U = 3$ eV and open boundary conditions.

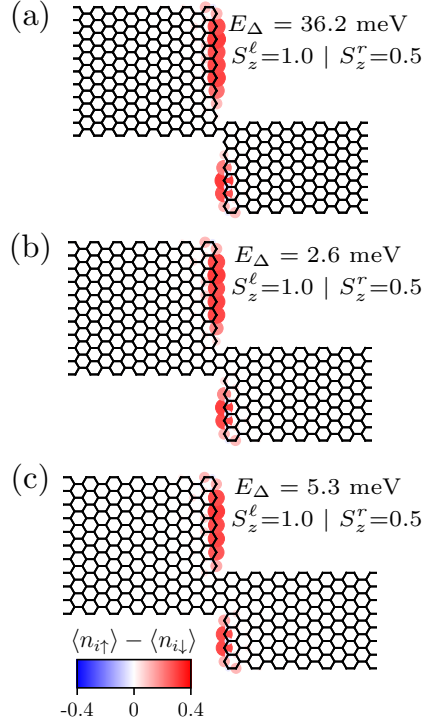


FIG. S12. Same as Fig. S11 but for a 21-15 junction.

-
- [1] L. Brey and H. A. Fertig, Electronic states of graphene nanoribbons studied with the dirac equation, Phys. Rev. B **73**, 235411 (2006).
 - [2] A. García-Fuente, D. Carrascal, G. Ross, and J. Ferrer, Full analytical solution of finite-length armchair/zigzag nanoribbons, Phys. Rev. B **107**, 115403 (2023).
 - [3] J. Lawrence, P. Brandimarte, A. Berdonces-Layunta, M. S. G. Mohammed, A. Grewal, C. C. Leon, D. Sánchez-Portal, and D. G. de Oteyza, Probing the magnetism of topological end states in 5-armchair graphene nanoribbons, ACS Nano **14**, 4499 (2020).

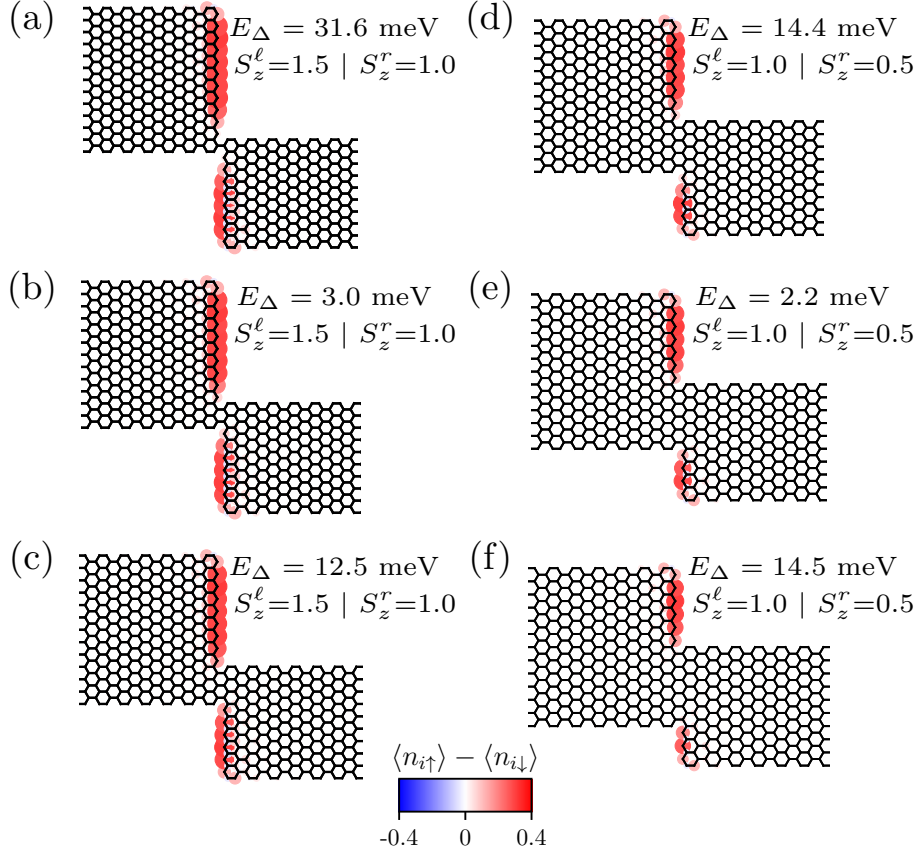


FIG. S13. Spin density distribution for the first excited state of a 25-19 heterojunction. The local spin moments $S_z^{\ell,r}$ and E_Δ are annotated in each panel. (a-f) Results for junctions with one to six C-C bonds at the interface, respectively. Size and color of the blobs at each site shows both the magnitude and sign of the spin polarization, as indicated by the inset colorbar, common for all panels.

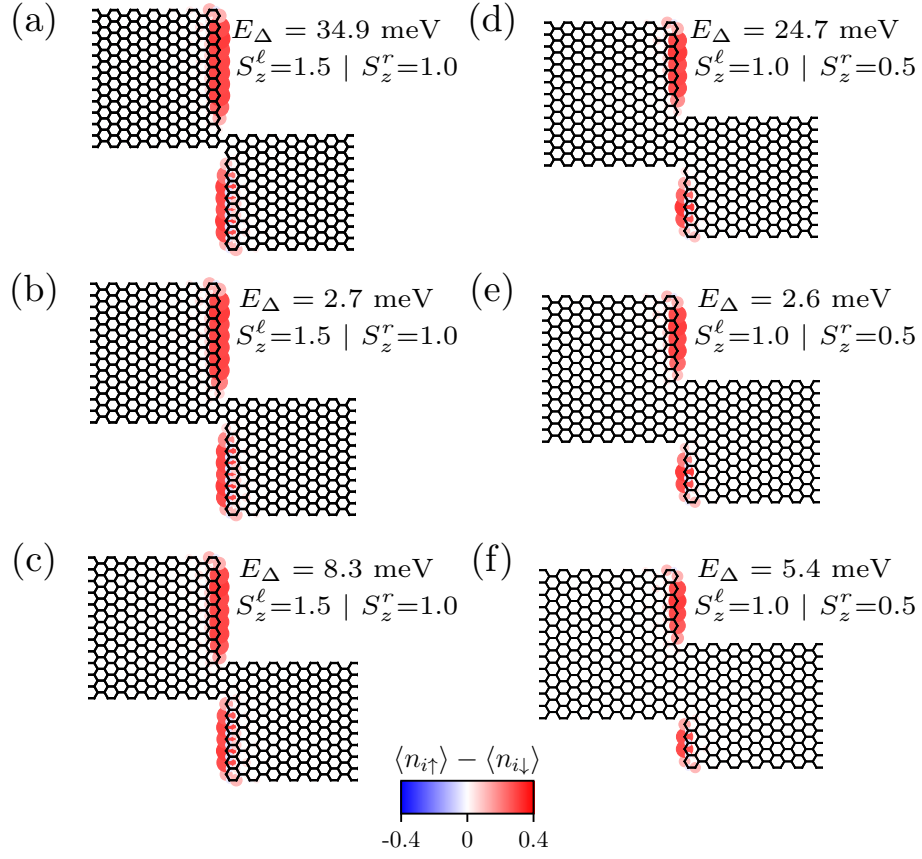


FIG. S14. Same as Fig. S13 but for a 25-21 junction.

